# Re-Assessment of Temperature-Dependent Strength, Strain Hardening, and Deformation Behavior in Binary Fe–Al Intermetallics

Jan Lars Riedel[a], Alexander Kauffmann[b]*, Stefan Guth[a], Marcel Muench[b], Georg Winkens[a], Daniel Schliephake[a], Jung Soo Lee[c], James P. Best[c], Frank Stein[c] and Martin Heilmaier[a]

[a] Institute for Applied Materials (IAM), Karlsruhe Institute of Technology (KIT), Engelbert-Arnold-Str. 4, D-76131 Karlsruhe, Germany

[b] Institute for Materials (IM), Ruhr University Bochum (RUB), Universitätsstraße 150, D-44801 Bochum, Germany

[c] Max Planck Institute for Sustainable Materials GmbH, Max-Planck-Straße 1, D-40237 Düsseldorf, Germany

* corresponding author
mail: alexander.kauffmann@rub.de (A. Kauffmann)
phone: +49 234 32 18430

## Abstract

Iron aluminides are promising structural materials for temperatures up to 700 °C. Among them, single-phase, *B*2-ordered iron aluminides containing 35 - 50 at.% Al are of particular interest due to their exceptional oxidation and sulfidation resistance. However, their use is limited by low ductility, primarily caused by environmental embrittlement, especially in alloys with >40 at.% Al, and vacancy strengthening. Despite extensive research, the understanding of the combined effects of point defects, environmental embrittlement, and deformation mechanisms across the entire Al range has been lacking. The present study addresses this gap by systematically characterizing the composition- and temperature-dependent mechanical behavior of a series of alloys with 30 to 53 at.% Al from room temperature (RT) up to 700 °C. Particular emphasis was placed on achieving uniformly low impurity levels and establishing similar heat-treatment conditions to reduce the strengthening effect of vacancies. Compression tests are employed to investigate the plastic deformation behavior and avoid premature failure. At RT, a minimum of hardness and offset yield strength is observed at 42 at.% Al, corresponding to the lowest vacancy and anti-site strengthening contribution. In the temperature range between 400–600 °C, a yield strength peak was observed for the alloys with 30 and 35 at.% Al related to the formation of $D0_3$-ordered domains (Fe-30Al) and strengthening effect by thermal vacancies (Fe-35Al). The continuously decreasing strain hardening capability with increasing temperature and Al content is rationalized by thermally activated processes, increasing vacancy concentration and localized plastic deformation.

## Keywords

Iron aluminides, B2 ordered structure, compression testing, Vickers hardness, Nanoindentation, deformation, strength

# 1. Introduction

Binary iron aluminides $Fe_xAl_{1-x}$ possess an outstanding corrosion and sulfidation resistance [1,2], a high density-normalized Young's modulus and low density compared to Ni-based superalloys [2,3]. Since they are made of affordable elements [4], they are suitable for applications like coal gasification [1], heat exchanger tubes, and protective coatings [3,5,6]. Considering the high recyclability and low energy consumption of Fe- and Al-based materials during recycling [7], FeAl alloys might serve as considerable substitutes for conventional materials, such as austenitic steels or high-Mn steels. Binary body-centered cubic (bcc)-based iron aluminides form different, disordered and ordered crystal structures depending on the Al content, which determine strength, strain hardening capability, hardness and plastic deformability. At room temperature (RT) [2], the *A*2-disordered crystal structure forms up to 18 at.% Al, the $D0_3$-ordered structure appears between 18 and 34 at.% Al, and the *B*2-ordered crystal structure forms at Al contents up to 50 at.% Al. The relevant part of the binary Fe-Al phase diagram (Fe-rich section) is shown in Figure 1. For high-temperature application, *B*2-ordered iron aluminides between 35 and 50 at.% Al are of particular interest as they are exceptionally oxidation and sulfidation resistant [1,2]. However, the suitable compositional range for structural applications is limited to approx. 42 at.% Al [2] – 48at.% Al [8] due to a lack of plastic deformability. Since the exact transition of application-relevant ductility is not yet entirely clarified, further studies are necessary. Furthermore, the underlying mechanisms determining the transition from brittle to ductile materials' response are unknown. The present study contributes to understanding the temperature-dependent strength and strain hardening behavior in the extended Al concentration range between 30 and 53 at.% Al as important contributions to the plastic deformation behavior. To avoid premature failure by crack formation and fracture, compression tests are applied to isolate the plastic response from embrittling factors.

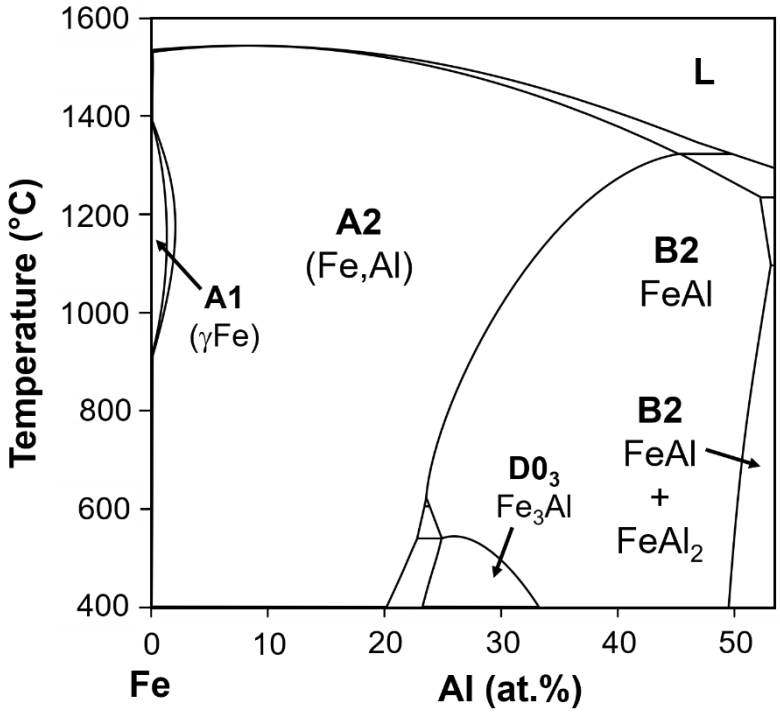


*Figure 1: The Fe-rich part of the Fe-Al phase diagram up to 53 at.% Al showing the liquid (L), A1, A2, B2, $D0_3$ single-phase fields and the $FeAl+FeAl_2$ two-phase field. Data taken from Ref. [9].*

The strength of iron aluminides at RT is rather low (~ 300 MPa for up to 48 at.% Al [10]) and strongly depends on the Al content [11] as well as on point defects like impurity solute atoms, vacancies and

anti-site atoms [10]. The temperature-dependent yield strength $\sigma_y$ of iron aluminides, which is divided into four regions, is shown in Figure 2 with:

- Region I: Strength decreases with increasing temperature by thermal activation of dislocation motion [12,13].
- Region II: Strength is dependent on the intrinsic lattice resistance.
- YSA Region ("Yield strength anomaly"): $\sigma_y$ can increase with increasing temperature for alloys with $< 47$ at.% Al by more than 100 MPa compared to $\sigma_y$ at RT (YS peak) [2,14–18].
- Region III: A drop of $\sigma_y$ occurs due to the onset of diffusion-controlled plastic deformation [13].

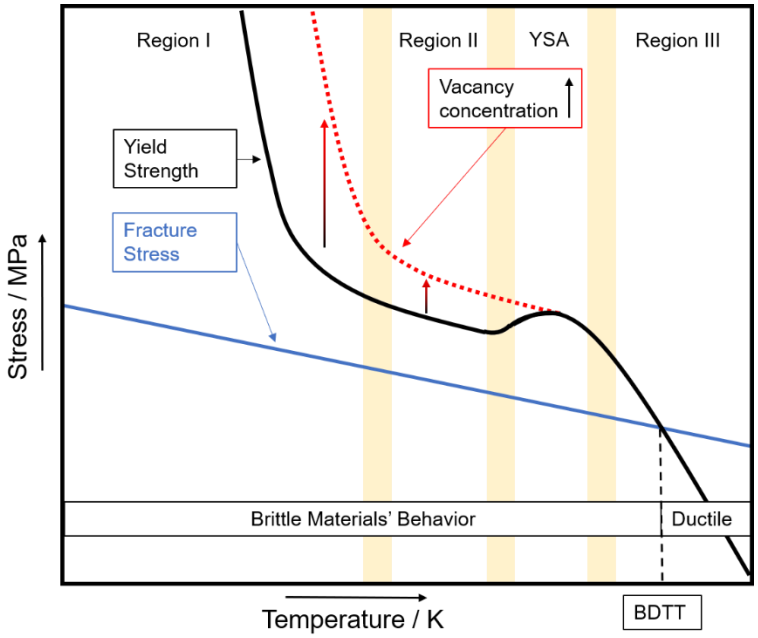


*Figure 2: Schematic temperature dependence of $\sigma_y$ and $\sigma_f$ of ordered iron aluminides adopted from Refs. [2,14,19]. The transition temperatures between two regions are visualized with yellow areas.*

Mechanical strength of iron aluminides in the regions I, II and the YS peak, as well as the hardness at RT, is sensitive to the concentration of vacancies [18]. Both, the hardness and strength are influenced by the heat treatment and cooling conditions [20]. Vacancies in *B*2-ordered FeAl alloys exhibit a low formation (~1 eV) and high migration enthalpy (up to 2.3 eV) [14,19]. Retained vacancies from heat treatment at high temperatures, for example 1000 °C, raise the hardness at RT and $\sigma_y$ within the regions I, II and YSA [2]. The observation of the YS peak is dependent on a vacancy-reducing heat treatment at 400 °C [2], as thermally generated vacancies at temperatures below the YS peak are considered to be the reason for the increase of $\sigma_y$. As a consequence, the strength is beyond the strength at the YS peak and therefore, the YS peak is not obtained in mechanical tests. Durations vary in the range of 100–120 h across different literature reports [19–22]. A YS peak has been reported for example for 120 h in Ref. [19]. This heat treatment at 400 °C for 120 h also yielded a reduction in RT hardness compared to a heat treatment at higher temperatures, as reported in Refs. [20–24] due to the removal of excess vacancies, enabling close to thermodynamic equilibrium conditions [25–29].

The determination of the temperature-dependent $\sigma_y$ as the onset of macroscopic plastic deformation can be obstructed in the case of brittle materials by premature normal fracture (cleavage) in tension. To circumvent the cleavage and premature failure of a specimen, compression tests can be utilized. As illustrated in Figure 2, the fracture stress $\sigma_f$ is less sensitive to a temperature increase, following mostly the decreasing trend of elastic stiffness. For brittle materials, it may be lower than the yield strength $\sigma_y$,

specifically at low test temperatures. Thus, a transition from brittle to ductile material behavior is observed, which defines the so-called brittle-to-ductile transition temperature (BDTT) [30]. Consequently, $\sigma_y$ is not directly accessible in tensile tests at temperatures below BDTT, as is for ordered iron aluminides, because they suffer from weak grain boundary cohesion [31,32] and inherent brittleness [33]. Notably, the BDTT for binary iron aluminides with up to 45 at.% Al has only been determined in four-point bending tests for alloys after casting [11], where a continuous increase with increasing Al content up to 42 at.% Al was found. For higher Al contents, a strong increase was reported in Ref. [11].

Interpreting temperature-dependent mechanical properties in iron aluminides can be challenging when the distinction between $\sigma_y$ and $\sigma_f$ in tension is not made explicit in the literature, specifically when the test temperature is close to or below BDTT. In several reports, the YS peak is associated with stress values that may potentially reflect $\sigma_f$ rather than the intrinsic onset of plasticity. For the temperature range in which the YSA is discussed, stress–strain curves are often not available, e.g. in Refs. [14–18], which makes it difficult to confirm yielding. This view is consistent with the fracture surfaces described in Refs. [8,15,17,18,34–47], which frequently exhibit brittle characteristics. Together, the observations raise the possibility that some reported stresses capture fracture limits rather than yield strengths. Accordingly, the mechanistic understanding of the YS peak and the temperature dependence of strength in these alloys remains partially incomplete. In addition, the mesoscopic microstructural changes induced by plastic deformation have been less systematically characterized.

The present study aims at generating appropriate datasets on $\sigma_y$ with the respective stress–strain curves, the analysis thereof and the microstructure after deformation over the entire Al concentration range of *B*2-ordered iron aluminides. Additionally, two alloys with Al concentrations below and above the *B*2-phase field are investigated. Specifically, the generation of the dataset is focused on (i) keeping consistent impurity concentrations between the different alloys and (ii) establishing comparable, defect-lean microstructural conditions by appropriate heat treatments. By utilizing the combination of compression tests, Vickers hardness measurements and nanoindentation experiments on iron aluminides cast from the same batch of raw materials, a comprehensive overview over the mechanical properties on the meso- and macroscale is provided. This approach enabled testing without the effect of premature sample failure due to low grain boundary cohesion, which is already caused at RT by environmental embrittlement [33,48], or a high BDTT [11]. It is relevant to note that environmental embrittlement is not entirely prevented when testing is carried out in controlled environments, such as in vacuum [32].

The present study gives a comprehensive overview on the plastic deformation behavior of FeAl alloys, which is not fully accessible in tensile tests due to low grain boundary cohesion, a high BDTT and environmental embrittlement. The experimental approach aims to clarify the following scientific questions:

1. How do mechanical properties, such as hardness, yield strength and strain hardening at RT up to 700 °C, of ordered FeAl alloys with Al concentrations between 30 and 53 at.% Al depend on temperature and composition?
2. What changes occur in the mesoscale microstructure depending on test temperature and alloy composition?
3. How does the temperature-dependent evolution of the mesoscale microstructure correlate with the mechanical properties of the alloys?

## 2. Materials and Experimental Methodology

The alloys used in this study with nominal compositions of 30, 35, 42, 47, 50 and 53 at.% Al were produced in a vacuum induction furnace (Balzers and Co., Bad Schönborn, Germany) from pure Fe (99.9 % purity) and Al (99.95 % purity) under Ar and cast into rectangular Cu molds with dimensions of $(200 \cdot 40 \cdot 180)\ \mathrm{mm}^3$. For all alloys, the same raw materials were used to keep the impurity contents comparable among the alloys.

The ingots were cut to cuboid compression test samples with the nominal size of $(3 \cdot 3 \cdot 5)\ \mathrm{mm}^3$ by utilizing a wire electric discharge machine (EDM), model BA24 supplied by Mitsubishi Electric Corporation (Tokyo, Japan). After EDM processing, the samples were ground to grit P1000 SiC paper to remove the oxidized surface layer followed by ultrasonic cleaning in ethanol. For the two-stage heat treatment process, the compression test samples were encapsulated into fused silica ampoules, which were evacuated and back-filled with Ar of 99.996 % purity for five times. To prevent Si diffusion from the fused silica into the specimens during heat treatment [49], the samples were wrapped in thin Mo-foil (ThermoFisher Scientific, Waltham Massachusetts, USA) before encapsulation. The heat treatment consisted of homogenization at 1000 °C ($0.73 \ldots 0.93 \cdot T_S$, solidus temperature $T_S$) for 48 h (except for Fe-53Al with 168 h to form a single-phase microstructure based on preliminary tests) with subsequent rapid cooling by dropping the ampoules into water. This procedure is followed by a low temperature heat treatment at 400 °C for 120 h also in ampoules to reduce excess vacancies [19] and again subsequent rapid cooling. A laboratory chamber furnace CWF1300 by Carbolite Gero GmbH & Co. KG (Neuhausen, Germany) was used for all heat treatments. The oxide scale on the samples was removed by grinding to P1000 SiC paper.

For microstructural investigations, a standard metallographic grinding and polishing procedure was applied. The sample surfaces were first ground with SiC paper to grit P4000. Subsequently, mechanical polishing was carried out utilizing a non-crystallizing oxide polishing suspension with pH = 7, particle size 50 nm (OP-S, Sommer Diamant Abrasive GmbH, Euenheim, Germany). This step was followed by chemo-mechanical polishing with a non-crystallizing oxide polishing suspension with pH = 9.8, particle size 40 nm (OP-S, Struers ApS, Ballerup, Denmark) to further remove the deformed layer after grinding. Finally, chemo-mechanical vibratory polishing was applied for 8 h utilizing a non-crystallizing oxide polishing suspension with pH = 9.8 (OP-S NonDry, Struers ApS, Ballerup, Denmark). For nanoindentation, the samples were mechanically polished up to 1 µm diamond suspension, followed by electropolishing using A2 electrolyte (Struers ApS, Ballerup, Denmark).

The crystal structure of the alloys was determined by X-ray diffraction (XRD) with a D2 Phaser device supplied by Bruker Corporation (MA, USA). For that purpose, compression test samples were mechanically crushed to powder at RT in an agate mortar. The voltage of the tube was set to 30 kV and the current to 10 mA. The Cu $K_\alpha$ radiation is filtered by means of a Ni foil and detected with a LynxEye line detector with a step size of 0.01° over the whole measuring range for $2\theta$ reaching from 10° to 145°. For each of the steps, the accumulated acquisition time was 384 s. For identification of the present phases, the diffraction patterns were evaluated with the open-source software PowderCell and compared to internationally accepted prototype information from the ICSD database. Lattice parameters were determined afterwards with a modified Nelson-Riley approach [50,51] based on the peak positions in the diffraction pattern.

The chemical composition was determined in the as-cast condition on compression test samples by means of inductively coupled plasma optical emission spectroscopy (ICP-OES) with an iCAP 7600 DUO analyzer (ThermoFisher Scientific, Waltham Massachusetts, USA), carrier gas hot extraction (CGHE) and combustion analysis (CA) with TC 600 and CS 600 devices, both supplied by LECO (St. Joseph, Michigan, USA). Backscattered electron (SEM-BSE) and secondary electron imaging (SEM-

SE) were performed utilizing a Leo 1530 field emission gun scanning electron microscope (SEM, Carl Zeiss AG, Oberkochen, Germany). SEM-BSE imaging was used for obtaining information about homogeneity by using atomic number contrast. In addition, SEM-SE contrast imaging was used for identification of topographic features such as pores and cracks. The acceleration voltage was set to 20 kV in all cases. Mesoscale deformation mechanisms were investigated by using an Auriga 60 focused ion beam field emission gun SEM (Carl Zeiss AG, Oberkochen, Germany) equipped with an EDAX DigiView electron backscatter diffraction system (EBSD, AMETEK Inc., Berwyn, USA). Data were acquired on an area of $(800 \cdot 800)\ \mu m^2$ in size at a step size of 2 µm and evaluated with MTex [52] in MATLAB.

Quasi-static compression tests were performed on a Z100 universal testing machine with an electro-mechanical drive supplied by ZwickRoell GmbH & Co. KG (Ulm, Germany). The machine is equipped with a three-zone vacuum furnace and temperature controller by Maytec GmbH (Singen, Germany). The heating rate was 10 K/min and the sample was held at the testing temperature for 30 min prior to testing. The initial engineering strain rate $\dot{\varepsilon}$ was set to $10^{-4}\ s^{-1}$. Hexagonal BN was used as a lubricant to reduce friction forces between samples' faces and punches. The temperature of the sample was measured during testing with a type S thermocouple, which was applied to the center of the sample. The atmospheric pressure inside the furnace was kept lower than $1 \cdot 10^{-4}$ mbar during all tests. For each temperature step, three compression tests were conducted to check reproducibility of test data.

The hardness of the alloys was evaluated utilizing compression test samples by using a Q10A+ semi-automatic Vickers hardness (HV) indenter from ATM Qness GmbH (Mammelzen, Germany) with a load of 1kg (HV1). A minimum number of ten indents within a random selection of grains were evaluated for statistical reasons. The minimum distance between two indents were at least three times the largest diagonal of the indents, the distance to the sample edges were at least six times the largest diagonal, according to DIN EN ISO 6507-1:2024 [53]. Nanoindentation was performed on different grains of the compression test samples with a distance of at least 30 µm from one indent to another (more than 25 times the maximum indentation depth) using a G200 nanoindenter by KLA Corporation (Milpitas, CA, USA). A diamond Berkovich indenter was used with a maximum indentation depth of 1 µm at a constant strain rate of $0.02\ s^{-1}$. Nine indents were performed on each grain. The analysis developed by Oliver and Pharr [54,55] was used to determine the nanohardness.

# 3. Results

## 3.1 Chemical Analysis and Initial Microstructure

The chemical composition of all alloys after casting was verified using ICP-OES, CGHE and CA. The results presented in Table 1 show that the actual alloy compositions closely align with the desired ones. Additionally, impurity levels are consistently low across the different alloys, which has previously been reported for this processing route in Ref. [16]. N and S were below the detection limit.

*Table 1: Chemical composition of the investigated alloys by ICP-OES (Al, Mn, Si) and CGHE (O, N) and CA (C, S). Fe is balanced.*

| Desired Al at.% | Al at.% | Al wt.% | Mn wt.ppm | Si wt.ppm | O wt.ppm | N wt.ppm | C wt.ppm | S wt.ppm |
|---|---|---|---|---|---|---|---|---|
| **30** | $30.1 \pm 0.7$ | $17 \pm 0.4$ | $347 \pm 7$ | $69 \pm 17$ | $12 \pm 3$ | < 10 | $65 \pm 5$ | < 20 |
| **35** | $34.8 \pm 0.9$ | $20.3 \pm 0.5$ | $332 \pm 10$ | $117 \pm 12$ | $99 \pm 27$ | < 10 | $55 \pm 3$ | < 20 |
| **42** | $41.4 \pm 1.2$ | $25.1 \pm 0.7$ | $310 \pm 9$ | $122 \pm 12$ | $163 \pm 33$ | < 10 | $9 \pm 1$ | < 20 |

| | | | | | | | | |
|---|---|---|---|---|---|---|---|---|
| **47** | 46.6 ± 1.3 | 29.5 ± 0.8 | 323 ± 9 | 140 ± 14 | 95 ± 35 | < 10 | 46 ± 4 | < 20 |
| **50** | 49.9 ± 1.3 | 32 ± 0.8 | 311 ± 6 | 138 ± 21 | 14 ± 4 | < 10 | 52 ± 5 | < 20 |
| **53** | 52.4 ± 1.4 | 34.4 ± 0.9 | 276 ± 8 | 151 ± 15 | 65 ± 21 | < 10 | 31 ± 5 | < 20 |

To investigate the microstructure following the homogenization at 1000 °C and subsequent low-temperature heat treatment at 400 °C, SEM-BSE micrographs were recorded and XRD measurements were conducted. Representative micrographs for all alloys are shown in Figure 3, while the XRD data are provided in the Supplementary Material (Figure S1).

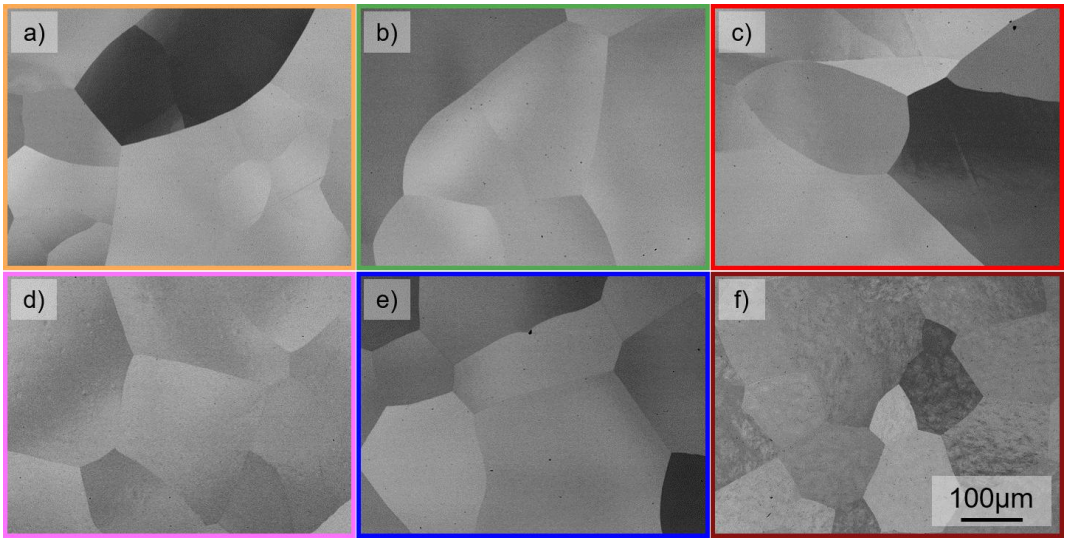


*Figure 3: The microstructure of iron aluminides after heat treatment at 1000 °C for 48 h (Fe-53Al: 168 h) and 400 °C for 120 h: a) Fe-30Al, b) Fe-35Al, c) Fe-42Al, d) Fe-47Al, e) Fe-50Al, f) Fe-53Al. The scale bar is the same for all images. Fe-53Al shows artefacts from preparation.*

All alloys exhibit grain sizes in the range of 200–300 µm. Apart from Fe-53Al, all alloys possess a homogeneous, single-phase microstructure at the micrometer scale. Based on the applied heat treatment at 400 °C and the phase diagram reported in Ref. [2], Fe-30Al is $D0_3$-ordered, while Fe-35Al, Fe-42Al, Fe-47Al, and Fe-50Al are single-phase *B*2-ordered. The crystallographic ordering in these four alloys increases with increasing Al content, i.e., Fe-35Al shows the lowest ordering and Fe-50Al the highest [56]. This characteristic is influential for mechanical properties, the presence of point defects and the defect structure itself [26–28,49,57–59], which will be discussed in detail in Section 4. Fe-53Al consists of *B*2-ordered FeAl and a secondary $FeAl_2$ phase [2]. The $FeAl_2$ phase is observed as lenticular features both within grains and along grain boundaries after 400 °C/120 h (Supplementary Material Figure S2 for more details).

## 3.2 Mechanical Properties

### 3.2.1 Hardness tests

The hardness is an indicator for vacancies retained in the alloys [60], if grain size and other microstructural parameters remain constant during different heat treatments. The Vickers hardness (HV) at RT after the homogenization at 1000 °C (HT) for 48 h (single-phase Fe-53Al with 168 h, shown in Supplementary Material Figure S3) is presented in Figure 4. Preliminary tests (not shown here) have shown that a duration of less than 168 h for Fe-53Al is insufficient for the dissolution of $FeAl_2$ phase, that formed during cooling after casting.

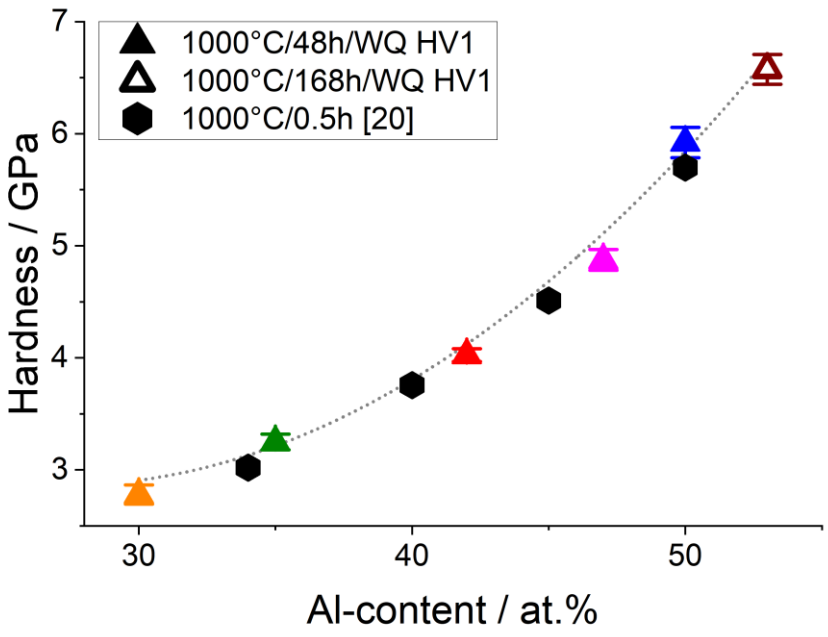


*Figure 4: HV as a function of alloy composition after a heat treatment at 1000 °C for 48 h (Fe-53Al: 168 h). For comparison, data from Ref. [20] are plotted as black hexagons. A dotted line is used as a guideline to the eyes. Data for this figure are available online [61,62].*

For samples with this heat treatment, the HV continuously increases with increasing Al content. This is consistent with the data published in Ref. [20] which is also included in Figure 4. In order to reduce the amount of thermal vacancies present in the alloys as much as possible [20], the alloys discussed here were subjected to a heat treatment at 400 °C for 120 h subsequent to the HT treatment. The results are presented in Figure 5. No cracks were observed after the Vickers indentation, as depicted for Fe-50Al in the Supplementary Material, Figure S4. A detailed discussion about the hardness is provided in Section 4.1.

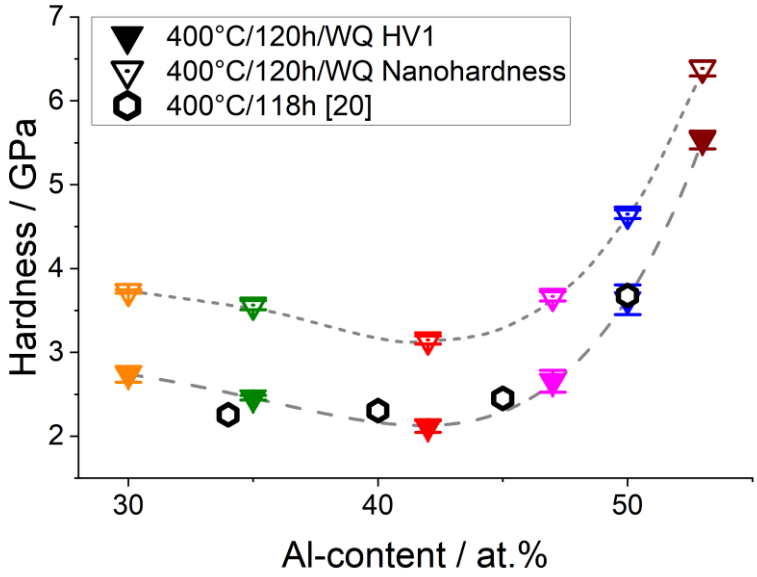


*Figure 5: HV and NH as a function of alloy composition after a heat treatment at 400 °C for 120 h. For comparison, data from Ref. [20] are plotted as black symbols. Dashed and dotted lines are used as a guideline to the eyes. Data for this figure are available online [61,62].*

### 3.2.2 Compression tests

To investigate the yield strength and strain hardening behavior independent of fracture and premature failure, compression tests were performed. Representative true stress–true strain curves for the alloys deformed at RT after a heat treatment at 400 °C for 120 h are presented in Figure 6a. The compression tests for the alloys with < 50 at.% Al content have been deliberately interrupted at (15 ± 1) % true strain, as marked by arrows, whereas the samples for Fe-50Al and Fe-53Al failed after reaching true strains of (15 ± 1) % and (8 ± 1) %, respectively. All data from the compression tests are publicly available [61,62].

The compressive stress–strain curves allow a quantitative assessment of the strain hardening behavior of the alloys without interference of premature fracture. The material's ability to homogenously deform plastic as one particular aspect of ductility can thus be investigated with limited obstruction by crack formation or grain boundary failure. For this, the room-temperature strain hardening behavior of the alloys is plotted in Figure 6b as Kocks-Mecking plots by showing true strain hardening $\mathrm{d}\sigma_\mathrm{t}/\mathrm{d}\varepsilon_\mathrm{t}$ as a function of true stress $\sigma_\mathrm{t}$ [63]. If there are no other crack-initiating mechanisms active, the corresponding strain, where $\mathrm{d}\sigma_\mathrm{t}/\mathrm{d}\varepsilon_\mathrm{t} = \sigma_\mathrm{t}$ is fulfilled, marks the upper limit of strain that the material might achieve via uniform plastic deformation *in tension* as the engineering relevant loading condition. Alloys with < 50 at.% Al have the potential to uniformly deform up to minimum 15 % strain. In contrast, the alloys with 50 and 53 at.% Al suffer from low strain hardening, a similar behavior to what has been published in Ref. [64]. The strain for Fe-47Al, where the $\mathrm{d}\sigma_\mathrm{t}/\mathrm{d}\varepsilon_\mathrm{t} = \sigma_\mathrm{t}$ criterion is met, is (15 ± 1) % (marked with a red dot in the figure). Fe-50Al and Fe-53Al fulfill the $\mathrm{d}\sigma_\mathrm{t}/\mathrm{d}\varepsilon_\mathrm{t} = \sigma_\mathrm{t}$ criterion at true strains of only (13 ± 1) % and (8 ± 1) %, respectively.

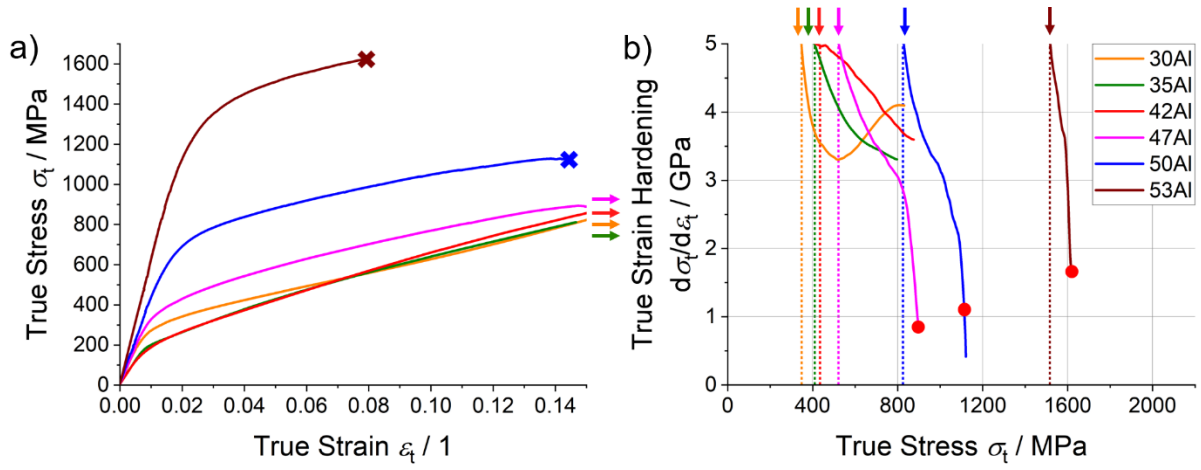


*Figure 6:a) Representative (selected) true stress–true strain curves for the alloys measured at RT after heat treatment at 400 °C for 120 h. Crosses mark tests with failed samples. The other tests were interrupted at $\varepsilon_t = (15 \pm 1)$ %, indicated by arrows. The initial engineering strain rate $\dot{\varepsilon}$ was set to $10^{-4}\ s^{-1}$. b) Kocks-Mecking plots derived from the tests shown in a). Red dots mark where $\sigma_t = \frac{d\,\sigma_t}{d\,\varepsilon_t}$ is met. Data for this figure are available online [61,62].The legend displayed in b) is for both micrographs.*

The RT 1 % and 5 % offset yield strength ($R_{\mathrm{p1}}$ and $R_{\mathrm{p5}}$) were determined for all alloys and are displayed in Figure 7 as a function of Al content. $R_{\mathrm{p1}}$ is used to assess yield strength from the continuous stress–strain curves obtained in this study. A larger offset strain compared to the often applied 0.2 % plastic strain criterion was chosen to avoid scatter of strength data by localization of plastic deformation in the early stages of compression in the coarse-grained material of the present study [65]. Additionally, $R_{\mathrm{p5}}$ allows to compare macroscopic strength data to hardness. Given the extent of plastic deformation and strain hardening during hardness measurements, a direct transformation of hardness into the yield strength is strictly not possible. However, the flow stress at 8 % plastic strain can be employed for an

assessment of the correlation of strength and hardness [66]. As Fe-53Al exhibited premature failure prior to reaching this strain level, the flow stress at 5% plastic strain $R_{p5}$ was utilized to remain consistent among all alloys [67]. The resulting correlation between $R_{p5}$ and HV (both for 400 °C for 120 h) is $R_{p5} = 0.26 \cdot HV$ (adjusted coefficient of confidence $R^2_{adj} = 0.99$). The correlation between $R_{p5}$ and NH is $R_{p5} = 0.20 \cdot H$ ($R^2_{adj} = 0.98$). Both correlations are shown in the Supplementary Material in Figures S5 and S6. The results on $R_{p1}$ at RT are consistent with the composition-dependent hardness presented in Figure 5 with a slight minimum of strength for Fe-42Al and a steep increase beyond Fe-42Al. Notably, enhanced strain hardening at intermediate Al concentrations covers the minimum of strength when $R_{p5}$ is solely assessed.

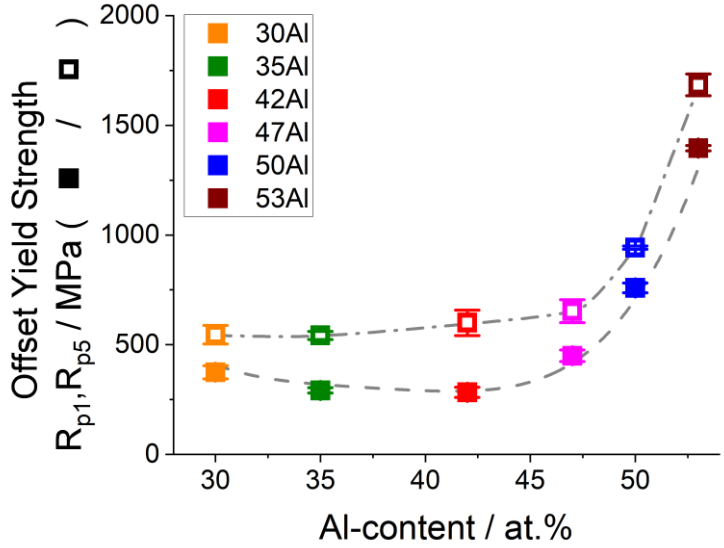


*Figure 7: $R_{p1}$ and $R_{p5}$ at room temperature as function of composition (closed squares for $R_{p1}$, open squares for $R_{p5}$). Error bars are smaller than the symbol size. Trendlines are shown as guidelines to the eyes. Data for this figure are available online [61,62].*

For the investigation of the high-temperature behavior of the alloys, compression tests have been carried out up to 700 °C in vacuum. Representative true stress–true strain curves for Fe-35Al and Fe-50Al are shown in Figure 8a and Figure 9a alongside Kocks-Mecking plots; for the other investigated alloys, the reader is referred to the Supplementary Material (Figures S7-S10).

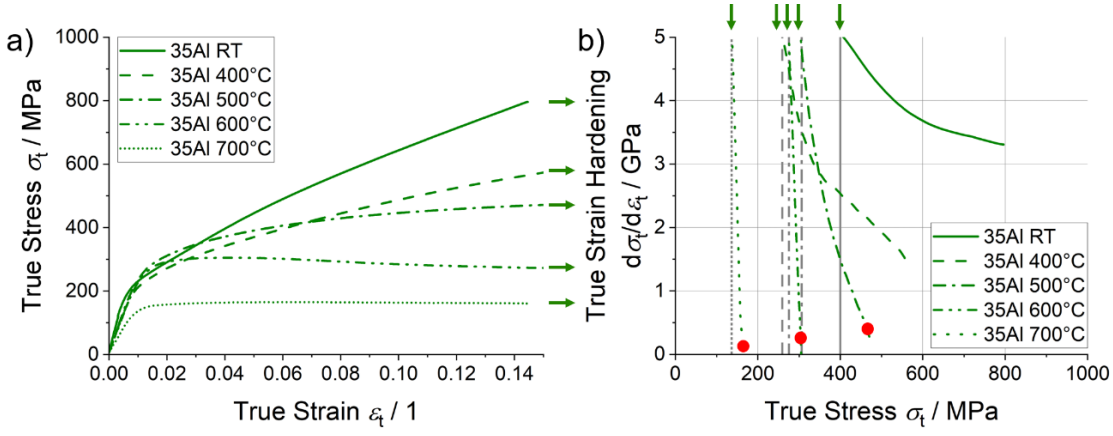


*Figure 8: a) Representative (selected) true stress–true strain curves for Fe-35Al at different temperatures. The tests were interrupted at $\varepsilon_t = (15 \pm 1)$ %, indicated by arrows. The initial engineering strain rate $\dot{\varepsilon}$ was set to $10^{-4}$ $s^{-1}$. b) Kocks-Mecking plots for the Fe-35Al deformed at different temperatures. Data for this figure are available online [61,62].*

The stress–strain curves of Fe-35Al reveal substantial strain hardening at temperatures up to 500 °C, which is the representative behavior for the alloys up to 47 at.% Al. The strain hardening is that high at RT and 400 °C that the maximum strain up to the interruption of test is insufficient to reach $d\sigma_t/d\varepsilon_t = \sigma_t$. The samples maintain an almost homogeneous stress state during testing due to the absence of necking and barreling during testing. As the $d\sigma_t/d\varepsilon_t = \sigma_t$ criterion is not reached during testing. Strain hardening is, thus, not limiting ductility up to 500 °C and Al concentrations of up to 42 at.%. For deformation at 500 °C, $d\sigma_t/d\varepsilon_t = \sigma_t$ is achieved at $(13 \pm 1)$ %. For even higher temperatures, the critical strains decrease to only $(3 \pm 1)$ %. Red circles in Figure 8b mark the points where the criterion is fulfilled. A substantially decreased strain hardening capability is obtained beyond 500 °C, corresponding to $0.46 \cdot T_S$ (for Fe-35Al). Furthermore, a maximum in the stress–strain curve is observed at 600 °C, indicating the onset of dynamic recovery or recrystallization [68]. Section 3.3 provides supporting experimental evidence on the onset of dynamic recrystallization.

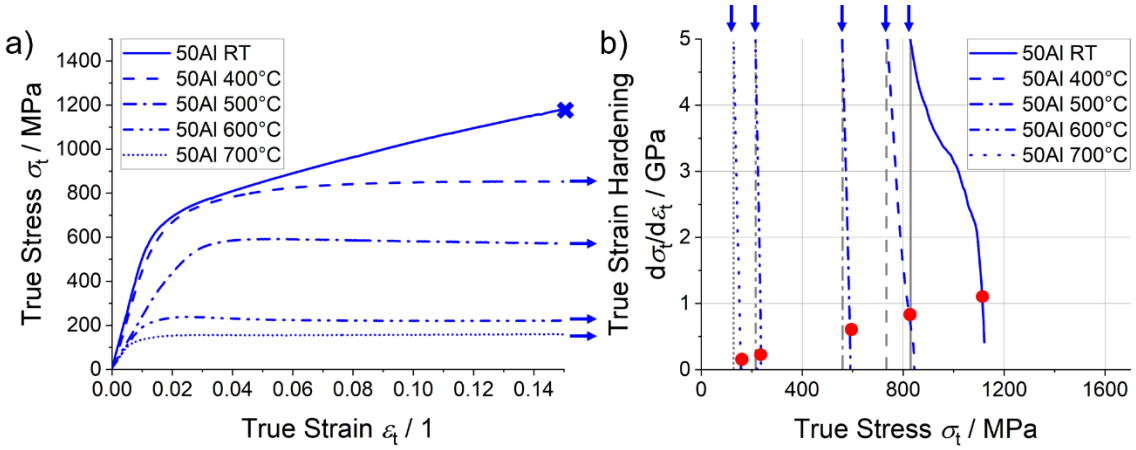


*Figure 9: a) Representative (selected) true stress–true strain curves for Fe-50Al at different temperatures. The test at RT failed at $\varepsilon_t = (15 \pm 1)$ %, indicated by a cross. All other tests were interrupted at $\varepsilon_t = (15 \pm 1)$ %, indicated by arrows. The initial engineering strain rate $\dot{\varepsilon}$ was set to $10^{-4}\ s^{-1}$. b) Kocks-Mecking plots for the Fe-50Al deformed at different temperatures. Data for this figure are available online [61,62].*

For Fe-50Al, the temperature-dependent behavior is different. Notable strain hardening is observed for RT and 400 °C, but to a lesser extent than for Fe-35Al as intergranular cracks are formed during deformation (displayed in Figure 12, see Section 3.3). This is discussed in more detail in Section 4. At higher temperatures, the strain hardening drops substantially. However, no maxima in the stress–strain curves are found. The samples fail at RT at a maximum strain of $(15 \pm 1)$ % with $d\sigma_t/d\varepsilon_t = \sigma_t$ being reached at slightly lower strain of 13 % (red points in Figure 9b). When deforming the alloy at higher temperatures, $d\sigma_t/d\varepsilon_t = \sigma_t$ is reached at true strains of $(10 \pm 1)$ % at 400 °C, $(4 \pm 1)$ % at 500 °C and only $(2 \pm 1)$ % at 600 °C and 700 °C, respectively. The onset of diffusion-controlled creep deformation is already noted at 400 °C ($0.44 \cdot T_S$ for Fe-50Al) compared to alloys with lower Al content due to the decreasing solidus temperature $T_S$.

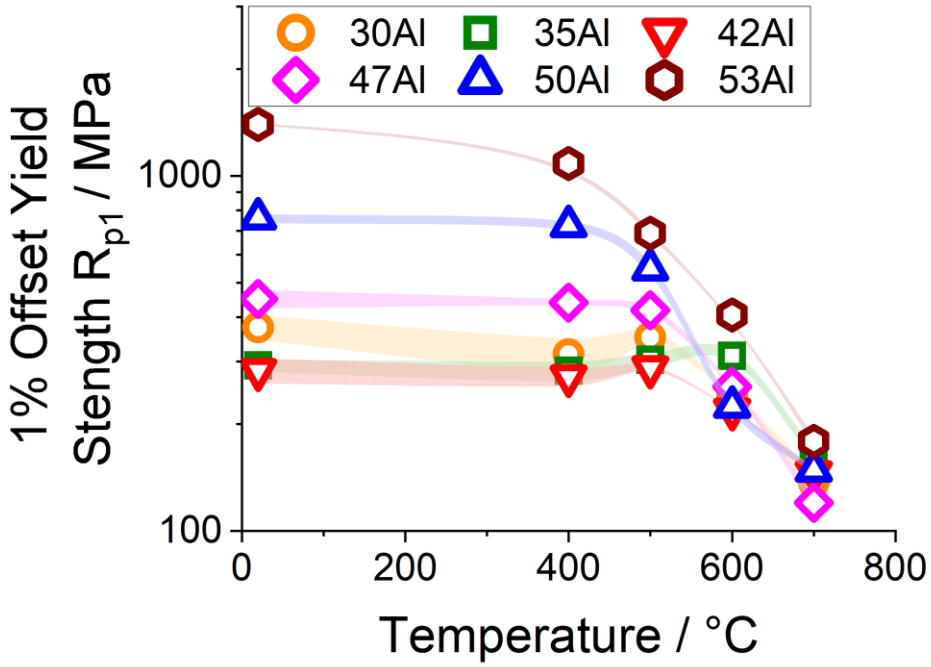


*Figure 10: The temperature and composition-dependent $R_{p1}$ of the iron aluminides investigated. Data for this figure are available online [61,62].*

Figure 10 displays the temperature-dependent $R_{p1}$ for all alloys after the heat treatment at 400 °C for 120 h between RT and 700 °C. Assessing Figure 10 against the temperature-dependent strength displayed in Figure 2, we can divide the temperature-dependent strength into three (Fe-30Al and Fe-35Al: four) different regions. The low-temperature regime displayed in Figure 2 with a low thermal contribution for overcoming the energy barrier against dislocation motion, is below the temperature range tested in the current investigation. Instead, RT is already within the temperature of the plateau region (indicated as region II in Figure 2), which reportedly starts at ~ $0.2 \cdot T_S$ [69] (RT is $0.17 \cdot T_S$ for Fe-30Al and $0.21 \cdot T_S$ for Fe-53Al). This plateau region extends to 400 °C ($0.39 \cdot T_S$, Fe-30Al and $0.44 \cdot T_S$, Fe-50Al) or 500 °C ($0.46 \cdot T_S$, Fe-35Al). The strength of Fe-30Al changes from $R_{p1}$ = (375 ± 30) MPa at RT, (314 ± 34) MPa at 400 °C to (351 ± 17) MPa at 500 °C, indicating the YSA region (see Figure 2). For Fe-35Al, the strength changes from $R_{p1}$ = (292 ± 12) MPa at RT to (282 ± 18) MPa at 400 °C, (303 ± 14) MPa at 500 °C and (311 ± 11) MPa at 600 °C. Data on the alloys other than Fe-30Al and Fe-35Al do not show indications for a YSA. A significant drop of strength (i.e., region III in Figure 2) for all alloys is observed at temperatures of 400–600 °C due to the onset of diffusion-controlled creep deformation at quasi-static strain rates. A detailed discussion about the strength is provided in Section 4.2.

### 3.3 Microstructure after Deformation

To investigate the deformation behavior, SEM-BSE micrographs were taken for all alloys at all temperatures discussed above after deformation to a true strain of (15 ± 1) %. As tests were deliberately stopped at this strain, potential cracks did not entirely propagate through the samples. The micrographs displayed in the present study were taken from the center section of the sample. This is demonstrated in the Supplementary Material, Figure S11 on one sample of Fe-35Al deformed at RT. The load direction is presented in each Figure once for all images depicted as a small rectangle (schematic of the compression test sample) with arrows (schematic for the applied load) pointing in the load direction. Figure 11 shows the microstructure of Fe-35Al as a representative low-Al alloy, while Figure 12 presents Fe-50Al as the same for high Al contents. The microstructure of the other alloys investigated are

presented in the Supplementary Material in Figures S12-S15. All alloys show indication of microscopic strain localization up to temperatures of 600 °C. The localization becomes evident in the form of lenticular features within the grains and is highlighted in the micrographs. For alloys with >35 at.% Al, intergranular cracks are observed. Fe-42Al displays these cracks up to testing temperatures of 400 °C, while the samples remain crack free at comparable plastic strain at higher temperatures. The transition temperature to crack-free deformation increases for Fe-47Al. For Fe-50Al, intergranular cracks were present even at the maximum testing temperature of 700 °C. As no cracks were observed in the as-processed microstructures, their formation and propagation are a response to the macroscopic deformation.

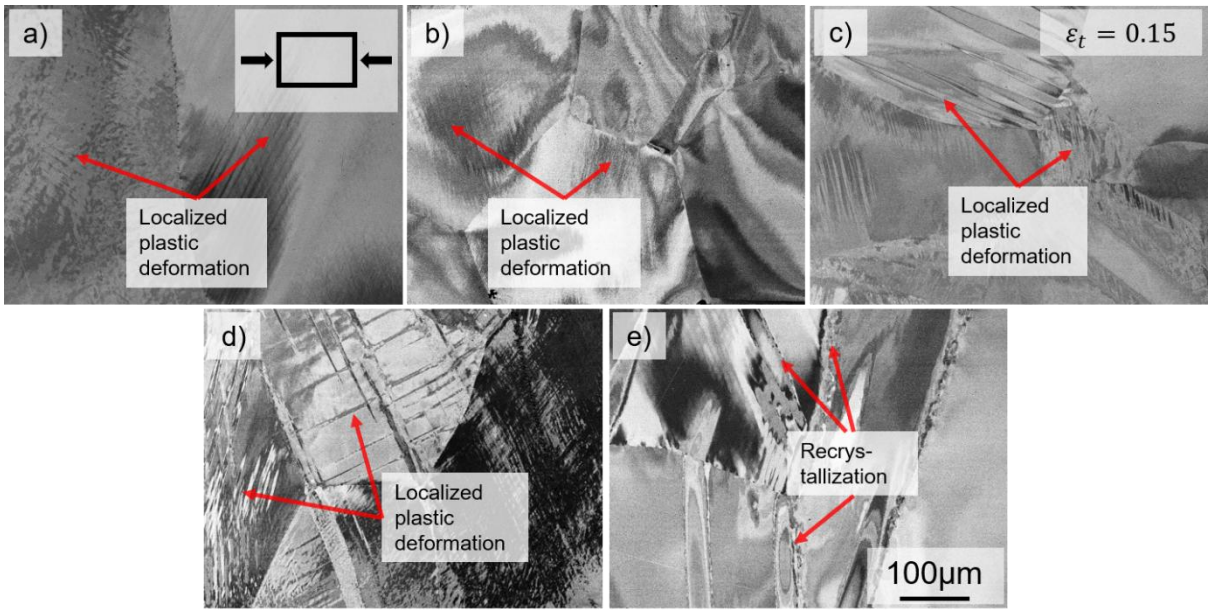


*Figure 11: The microstructure of Fe-35Al after deformation to* $\varepsilon_t = (15 \pm 1)$ % *at different temperatures: a) RT, b) 400°C (*$0.40 \cdot T_S$*), c) 500°C (*$0.46 \cdot T_S$*), d) 600°C (*$0.52 \cdot T_S$*), and e) 700°C (*$0.57 \cdot T_S$*). The scale bar is the same for all images. The compression direction is horizontal.*

Consistent with the maximum of the true stress–true strain curve at 700 °C in Figure 8a and S8, the onset of dynamic recrystallization is microstructurally verified by new grains formed as necklace structure at the former grain boundaries of alloys with <47 at.% Al. Dynamic recrystallization is not completed due to too low temperature and limited plastic strain applied in the interrupted compression tests. The alloys with higher Al contents do not show evidence for dynamic recrystallization. Fe-53Al shows $FeAl_2$ formation on grain boundaries at 600 °C and 700 °C in addition to the absence of cracking.

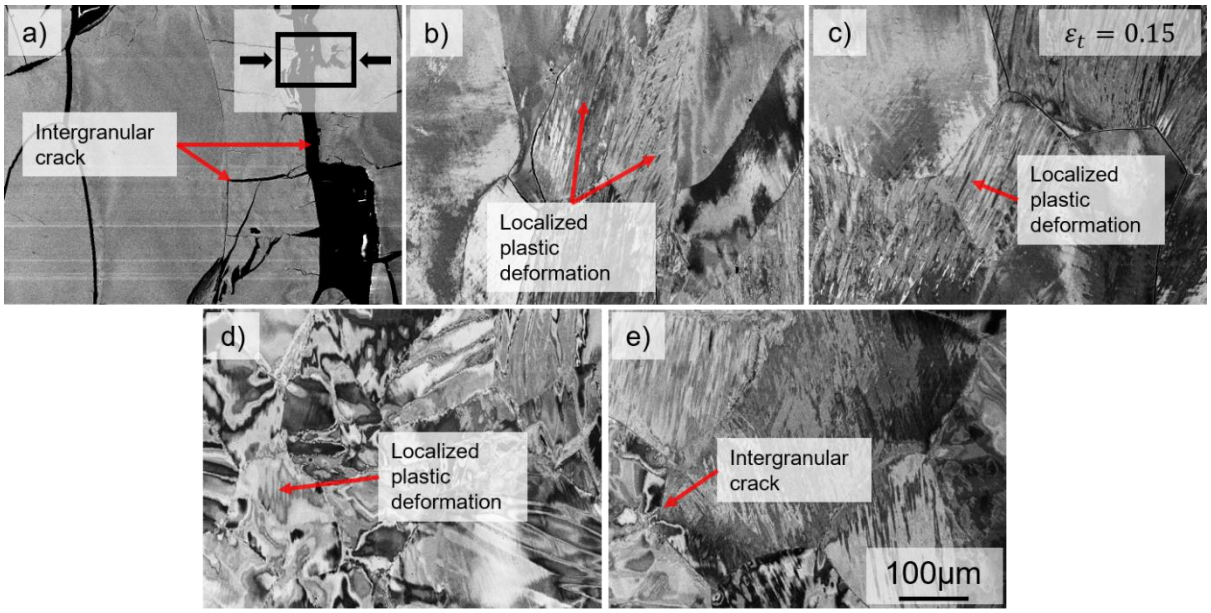


*Figure 12: The microstructure of Fe-50Al after deformation to* $\varepsilon_t = (15 \pm 1)$ % *at different temperatures: a) RT, b) 400°C (*$0.44 \cdot T_S$*), c) 500°C (*$0.51 \cdot T_S$*), d) 600°C (*$0.58 \cdot T_S$*), and e) 700°C (*$0.65 \cdot T_S$*). The scale bar is the same for all images. The compression direction is horizontal.*

The occurrence of intergranular fracture for the alloys with >35 at.% Al is attributed to environmental embrittlement at ambient temperatures, which mainly occurs for alloys with >40 at.% Al [33,48]. For this, Al in FeAl alloys reacts with moisture in ambient air and forms a protective alumina scale. The resulting atomic H diffuses into the material and causes brittle failure [4,33,48]. As outlined in Ref. [48], testing in vacuum, as is done in the present study, does not entirely prevent this effect. The exact mechanism how H affects the grain boundary cohesion of the material is still controversial and only to be resolved with micro-mechanical testing methods, as discussed in Ref. [4].

The deformation bands seen in the SEM-BSE micrographs show a change in contrast, which indicates a change in crystallographic orientation within the bands. This orientation change was quantitatively analyzed by SEM-EBSD to verify the formation of kink bands (KB). To improve statistical relevance, orientation analysis was carried out for multiple KBs. One example is displayed in Figure 13 and described in the following, while additional data can be found in the Supplementary Material in Figures S16 and S17.

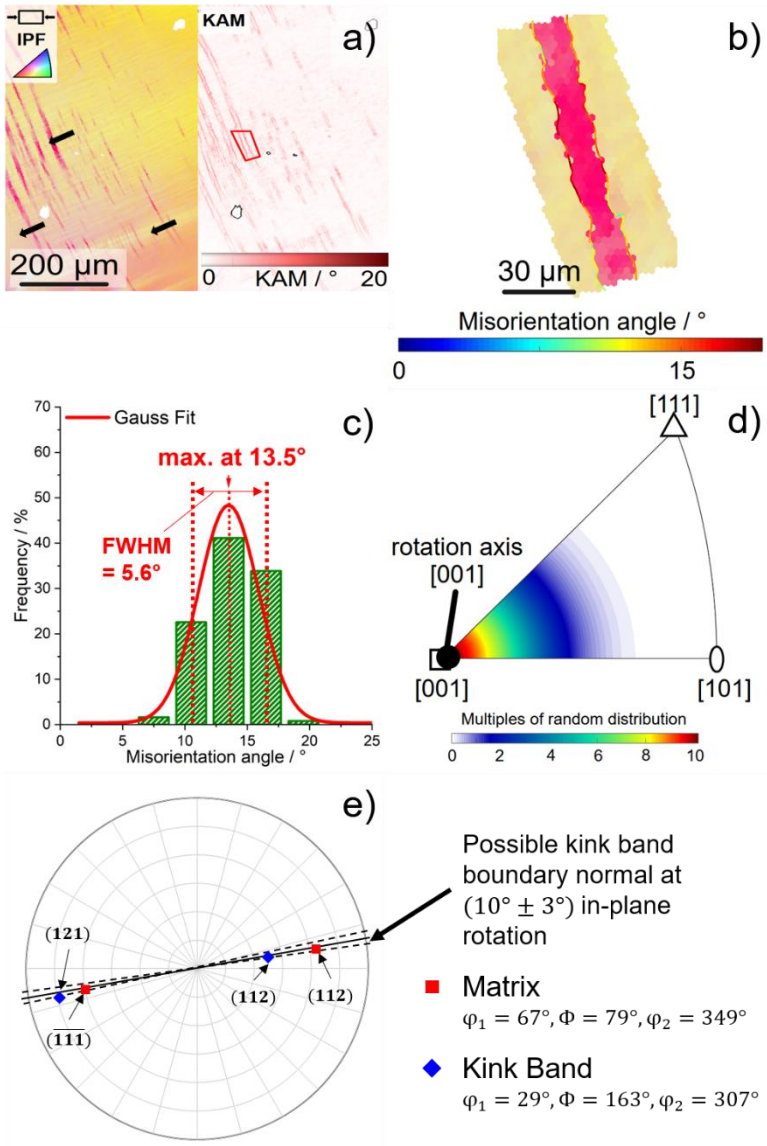


*Figure 13: Properties of KBs for Fe-35Al after deformation at 600 °C. a) region of interest (ROI) as an orientation map (left) with respect to compression direction (the color code of orientations corresponds to the IPF in the inset in the left upper corner) and kernel average misorientation (KAM) map of the identical area (right). Black arrows highlight KBs. b) Misorientation angle distribution along the boundary of an individual kink band highlighted by the red polygon in a). c) Relative frequency distribution of misorientation angles (histogram) from b). A Gauss fit is plotted as line in the diagram. d) Orientation distribution of rotation axes determined from b) presented as colored map in an IPF. e) Stereographic projections from the orientations obtained in a) including the possible slip planes (kink band interface normal vectors) highlighted as black lines. Eulerian angles in Bunge notation.*

Figure 13a (left) displays the inverse pole figure (IPF) map of KB in a grain of Fe-35Al deformed at 600 °C up to a true strain of (15 ± 1) %. The KAM map presented in Figure 13a (right) visualizes the local misorientation at the boundaries of the KBs. One individual band was picked for further analysis, highlighted by a red polygon in the KAM map. Varying shades of red color along the kink band boundaries reveal a varying misorientation against the matrix, which is also displayed in Figure 13b in the magnified image of the band. The color-coded misorientation angle along the kink band boundary revealed misorientation angles between 9° and 21°. The relative frequency distribution of these angles (bin size of 3°) is plotted in Figure 13c. The frequency maximum of 13.5° and full width at half maximum (FWHM) of 5.6° ($R^2_{\mathrm{adj}} = 0.87$) were determined using a Gauss function fit to the distribution. The frequency distribution of rotation axes (Figure 13d) within the individual band as depicted in the IPF map of Figure 13b reveals a maximum in the ⟨001⟩ direction. For identifying the most probable slip

plane, the KBs were analyzed similar to the procedure described in Ref. [70]. The intersection of the boundaries of the KB with the surface are found at angles close to $(10 \pm 3)°$ with respect to the compression direction in the image plane (horizonal, see Figure 13a). The corresponding plane normal of the interface between KB and matrix is then found on a trace at about 10° from the center of the pole figure in Figure 13c. For the particular KB in Figure 13, the interface would be consistent with various {112} or a {111} plane. If the kink band is formed by the massive operation of a single slip system, the interface between KB and matrix would be congruent with the active slip plane.

Based on the results on all KBs, the following statements can be concluded. The misorientation with respect to the surrounding grains widely ranges from 8° to 16.5°. Neither a uniform rotation axis nor a uniform slip system can be identified from the features analyzed in differently orientated grains, suggesting that different slip systems are active and lead to localization of plastic deformation. A detailed discussion is provided in Section 4.3.

# 4. Discussion

The manufacturing of samples made of binary iron aluminides is crucial when it comes to the assessment of mechanical properties, as it affects the chemical homogeneity and impurity contents. The effects of (i) accuracy of the chemical composition as well as (ii) chemical inhomogeneity following synthesis can be estimated when evaluating the RT hardness (Figure 5) and $\sigma_y$ (Figure 7) of chemically homogenous Fe-Al alloys. A variation of the Al content by a few atomic percent leads to a significant change in hardness and strength, especially for alloys which contain > 42 at.% Al, for example a spread of 1.5 GPa in HV and 460 MPa in $\sigma_y$ in Fe-(47 ± 3)Al, respectively. (i) With respect to the accuracy of the actual composition (in comparison to the desired composition), some studies from literature do not disclose experimental verification which needs to be considered in comparisons [14,15,17,18]. In the present study, the maximum experimentally verified deviation of –0.6 at.% Al (Fe-42Al and Fe-53Al) are well below the standard deviations (~ 1 at.%) of the chemical composition determination by ICP-OES. Thus, the deviation is considered as minor. The impurity levels are small and the slight variations among the alloys investigated in this study are considered negligible for the trends observed for hardness and strength as a function of Al concentration. (ii) Chemical homogeneity needs to be considered for example when assessing Ref. [11] dealing with the composition-depending BDTT obtained on the as-cast condition without further homogenization treatment. Other studies that are used for the comparative assessment in the following, rely on homogenization treatments at temperatures between 850 °C [18] and 1200 °C [14–17,20]. However, durations are either undefined [17] or vary between 10 min and 10 h [14–16,18,20]. The microstructural investigations by SEM-BSE (Figure 3 and Figure S1, SEM-EDS not shown here) experimentally prove the chemical homogeneity on the micrometer scale of the alloys synthesized in the present study with a 1000 °C/48 h homogenization treatment (Fe-53Al for 168 h at the same temperature, Figure S3).

Apart from the chemical composition, grain size might affect the assessment of mechanical properties, for example with respect to strength and hardness by grain boundary strengthening or with respect to fracture stresses by weak grain boundaries in experimental studies from literature using tensile tests. The grain sizes after the processing of the alloys were mostly reported to be in the range of 200–400 µm in literature [15,17,18,20] similar to the grain sizes obtained in the present study. Thus, these studies are comparable with the present one. Compared to the sample size, these large grain sizes contribute to the scatter obtained for the strength data shown in Figure 7 and Figure 10 by favorable orientation of selected grains in some specimens [71]. This statistical variation upon testing of multiple samples per condition is deliberately characterized by the uncertainty ranges and bands included in the Figures of the present study. Considering the anticipated dependencies on composition and temperature, the scatter

is small. Across all length scales, macroscopic testing, hardness and nanohardness yield consistent results. The latter two are lean or even free of significant influences by grain boundaries. The number of samples tested as well as scatter ranges often remain undisclosed in literature, for example Refs. [14–18], which precludes a deeper assessment of this factor in comparison to literature.

### 4.1 RT Hardness and Strength

Immediately after the completion of the homogenization treatment at 1000 °C, high point defect concentration and, thus, high hardness is observed [60]. This is consistent with hardness reported in literature Ref. [20]. It is to be noted that further mechanical characterization is impossible in this processing condition due to brittleness, independent of the alloy composition. Even testing in compression leads to catastrophic failure within the elastic range and with enormous scatter of fracture stress (not shown here).

To assess the materials' intrinsic properties, a point-defect reducing heat treatment at 400 °C for 120 h has been performed, leading to a lower hardness for all tested alloys, enhanced ductility and increasing crystallographic order. Comprehensive experimental evidence for the reduction of point defects within the alloys is documented in literature, see Ref. [20–29,58,72]. The high homologous temperature during homogenization leads to the formation of completely recrystallized and recovered grains, as shown by the continuous contrast in the SEM-BSE images in Figure 3. The initial dislocation density after the heat treatment at 400 °C is low, as it was shown in Ref. [64], and the strengthening contribution of dislocations compared to vacancies is minor [24]. Similarly, the effect of strengthening through anti-phase boundaries, which are found to be present in alloys with Al contents <32 at.%, is negligible [24,73]. Figure 4 and Figure 5 present the Vickers hardness after homogenization at 1000 °C and subsequent aging at 400 °C, respectively, along with data from Ref. [20]. The trend of Vickers hardness obtained after homogenization at 1000 °C and aging at 400 °C is consistent with the results reported in Ref. [20], despite slight differences in the duration of the thermal treatments (homogenization at 1000 °C/0.5 h [20] vs. 48 h in the present study and 400 °C/118 h [20] vs. 120 h, respectively). The trends observed in HV, NH, and $\sigma_y$ in the present study reveal a local minimum at 42 at.% Al, followed by a pronounced increase for higher Al concentrations. After the heat treatment at 400 °C, different defect structures exist in FeAl alloys. Prior studies in Refs. [26–28,49,57–59,74] and the phase diagram in Ref. [75] show that alloys with <38 at.% Al are mainly governed by single vacancies due to low crystallographic ordering, while alloys between 38–50 at.% Al predominantly contain triple defects (i.e., two vacancies on the Fe-sublattice and one Fe anti-site atom) are the main defects. The exact strengthening contributions of both defect structures are not yet resolved, as triple defects and vacancies are both formed with increasing Al content [20]. Each defect type is present across the *B*2-phase field but becomes dominant in the corresponding sub phase fields depicted in the Ref. [75]. Single vacancies, having low migration enthalpies, are removed quickly at low temperatures, whereas triple defects require longer times due to higher migration enthalpies [76]. Anti-site defects are also of importance in FeAl, which increase linearly with decreasing Al content (decreasing crystallographic order) [26]. Anti-site atoms are present in high concentrations independent of temperature [57], e.g., up to 20% in Fe-40Al, as shown in Ref. [26]. The strengthening contribution of anti-site atoms is smaller than that for vacancies [60,77]. After the heat treatment at 400 °C, Fe-30Al shows no change in hardness (2.7 ± 0.1) GPa, consistent with [57], which reports nearly temperature-independent vacancy and anti-site concentrations. Fe-42Al exhibits the lowest HV, NH, and $\sigma_y$ after 120 h, reflecting reduced anti-site strengthening due to higher crystallographic ordering [26]. The gradual hardness decrease from Fe-35Al to Fe-42Al suggests that the transition from single vacancies to triple defects has only a minor effect on mechanical properties. For Al contents >42 at.%, vacancy strengthening becomes dominant [27,60]. Thus, the lowest hardness of Fe-42Al arises from minimal contributions of both, anti-site [57] and

vacancy strengthening [29,78], a trend also confirmed by strength measurements at 400 °C. This implies that the minimal strength is indeed no artifact of temperature (i.e., different onset temperatures of Region II in Fig. 2), but instead caused by temperature-independent parameters, such as the anti-site atom concentration. The results obtained from nanohardness (NH) measurements with much smaller probed volume verify the behavior obtained in Vickers hardness measurements. Still, the values of NH are higher because of the indentation size effect [79]. The RT strength displays the same behavior as the HV because of an increasing contribution of anti-site atoms to the strength of Fe-30Al, and a minimal anti-site and vacancy strengthening contribution for Fe-42Al. The same trend for the RT strength was presented in Refs. [15–18]. In Ref. [16], where the lowest strength was observed at 40 and 45 at.% Al, the absence of intermediate compositions precluded precise identification of the minimum. $\sigma_y$ at RT obtained in the present study is comparable to the strength reported in Ref. [16] for 40–52 at.% Al, both in terms of magnitude and composition dependence. The alloys in Ref. [16] were processed via a similar route and with similar impurity contents. Also, the absolute strengths reported in Refs. [15,17,18] match those in the present study up to an Al content of 46 at.% ranging from 250 to 320 MPa. However, deviations were found at higher Al contents, specifically at 48 at.% and 50 at.% Al. The strength at RT was reported to be around 300 MPa at 48 at.% Al (vs. Fe-47Al with 450 MPa from the present investigations), and 1 GPa at 50 at.% Al (vs. Fe-50Al with 760 MPa) [17]. These differences can be explained by deviations in chemical composition (experimentally not verified in Ref. [17]) as outlined above.

## 4.2 Temperature-Dependent Strength

Considering the experimental uncertainties in the present study, only the alloys with 30 and 35 at.% Al demonstrate a YS peak. This observation was made despite application of a point defect reducing heat treatment that is considered as a pre-requisite for the occurrence of the YS peak in literature. This contradicts earlier reports suggesting the presence of a YS peak up to 47 at.% Al in tension [14,15,17,18] and compression [16]. However, the results presented in Refs. [14–18] lack a consistent distinction between $\sigma_y$ and $\sigma_f$. This may lead to recorded temperature-dependent stresses not necessarily only related to the onset of plasticity but involving crack formation and related anomalies of the data. Furthermore, Refs. [14,16–18] do not contain stress–strain data and, thus, do not allow for an re-assessment of the onset stresses. Consequently, the assessment of a YS peak necessitates the exclusive consideration of $\sigma_y$, as presented in this study employing compression testing and post-deformation microstructural investigations to confirm the activation of plastic deformation and the absence of cracking.

To rationalize the occurrence of the YS peak in Fe-30Al and Fe-35Al observed in the present study, several factors must be considered. Consistent with Ref. [26], Fe-30Al shows no dependence of RT hardness on prior heat-treatment temperature, indicating that vacancies do not significantly strengthen this alloy. Fe-35Al exhibits a slight RT hardness difference after heat treatments at 400 °C and 1000 °C (less than 0.7 GPa), attributed to minor vacancy strengthening. For Al contents greater than 35 at.%, the strengthening contribution by vacancies is substantial with more than 2 GPa RT hardness difference after heat treatments at 400 and 1000 °C.

In Ref. [80], the effect of the heat treatment temperature on the strength of a multi-component Fe-28Al-Cr-Mn-Si was investigated. After different heat treatments in the temperature range between 380 and 520 °C for different dwell times, the lowest strength was found at 380 °C and the highest at 510 °C. Transmission electron microscopy (TEM) investigations in Ref. [80] showed that this increase in strength between 380 °C and 510 °C is attributed to the growth of $D0_3$-ordered domains in the $B2$ matrix, with the interfaces inhibiting dislocation motion. In the present study, the strength increases by ~50 MPa between 400 °C and 500 °C for Fe-30Al. In Ref. [80], a comparable increase in strength of about

100 MPa (380 vs. 510 °C) is observed after a 30 min dwell time (chosen to match the dwell period used prior to testing in the present study). Differences are due to the different alloy compositions (multi-component in Ref. [80] vs. binary in the present study) and temperatures for the heat treatments. For Fe-35Al, the occurrence of the YS peak is explained by the strengthening contribution of thermally generated vacancies. According to Ref. [19], the RT strengthening effect by vacancies can be estimated using

$$\Delta\sigma = \beta\, G \sqrt{x_V} \quad (1)$$

whereby $\beta$ denotes a factor smaller than unity ($\beta$ = 0.076 in the work of [60]), G is the shear modulus (G = 100 GPa according to Ref. [19]) and $x_V$ as the vacancy concentration. Utilizing a vacancy concentration (Fe-36Al) as well as linear extrapolation (to temperatures lower than 800 K), both from Ref. [49], a change in $x_V$ of about $1.5 \cdot 10^{-5}$ can be estimated. With this, the increase in strength $\Delta\sigma$ amounts to about 30 MPa, matching with the results in the present study. For Al contents higher than 35 at.%, the very strong vacancy strengthening even after vacancy reduction heat treatments is strong enough to raise the plateau strength (Region II in Fig. 2) beyond YS peak strength effectively covering the phenomenon.

### 4.3 Temperature-Dependent Microstructure Evolution and Strain Hardening

The post-deformation, mesoscale microstructure documented in the present study, including the formation of kink bands, has previously not been reported in literature for iron aluminides. Kink bands represent a localization of plastic deformation and are observed at temperatures up to 700 °C. However, deformation bands in general are considered to disappear at elevated temperatures as more slip systems become activated. This would enhance homogeneous deformation and localized plastic deformation becomes less pronounced [68,81–83]. The opposite trend obtained for iron aluminides might be related to the reported change in the active slip direction from ⟨111⟩ below to ⟨100⟩ above $0.5 \cdot T_S$, respectively [84–86]. This corresponds to a reduction in the number of independent slip systems. The increasing occurrence of kink bands in Fe-35Al at 600 °C ($0.52 \cdot T_S$) compared to lower temperatures, suggests that the decreasing strain hardening is connected to the strong localization of plastic deformation. Still, the statistical analysis of KBs in the present study (Figure 13 and Figures S16 and S17) did not yield a unique set of slip systems consistent with the known slip systems [84–86].

After the deformation at 700 °C up to 15 % strain, the onset of dynamic recrystallization was verified for alloys with < 47 at.% Al, even though these alloys possess lower homologous test temperatures than the ones with higher Al content. An entirely recrystallized microstructure is expected for larger total strains as reported in Ref. [68]. The absence of dynamic recrystallization for alloys with higher Al contents might be rationalized by the increasing vacancy concentration in $B2$-ordered FeAl [60]. A higher vacancy concentration can increase the probability for dynamic recovery by dislocation annihilation as a competing mechanism to recrystallization. This was shown for example in Ref. [87] for stoichiometric FeAl or Ref. [88] for a non-binary Fe-40Al alloy. Another possible origin is the reduction in grain boundary mobility and therefore retardation recrystallization when atomic ordering becomes more pronounced [68]. As dynamic recrystallization is dependent on total strain and strain rate [68], either of the two might be too low to achieve dynamic recrystallization at the temperatures tested.

These microstructural changes are linked to the trends observed in the temperature-dependent strain hardening capability. At temperatures of ~ $0.4 \cdot T_S$, thermally activated processes such as dislocation cross slip (screw dislocations) and diffusion-controlled climb (mixed and edge dislocations) become active [85] and contribute to dynamic recovery by enhanced dislocation annihilation. With increasing Al content, $T_S$ decreases and therefore, these mechanisms are observed at lower absolute temperatures.

In addition, the amount of vacancies increases with increasing Al content [10], which promotes the diffusion-controlled climb. In the present study, Fe-35Al shows a high strain hardening capability up to 500 °C, whereas no strain hardening is observed for Fe-50Al at temperatures higher than RT. The high strain hardening capability of FeAl alloys with Al contents <43 at.% may also be correlate to the formation of jogs due to the interaction of glissile dislocations with forest dislocations, as shown in Refs. [89–93]. Following this, extended dipoles are formed, which eventually form dislocation loops. Both effectively contribute to strain hardening by increasing the dislocation density. These studies are limited to FeAl alloys with <43at.% Al [89–93] due to the limited tensile ductility of alloys with higher Al content. Further TEM studies on the compression tested specimens from the present study will allow for the assessment of these dislocation-interaction-related aspects also for higher A contents. Apart from dynamic recovery, the localization of plastic deformation by kink band formation might contribute to the continuously decreasing strain hardening capability with increasing temperature.

## 5. Conclusion

The present study focused on the hardness, strength and strain hardening of binary FeAl alloys within the compositional range of 30 to 53 at.% Al at temperatures up to 700 °C. All alloys were cast from the same batch of raw materials and subjected to the same heat treatment at 400 °C for 120 h. This approach enabled the analysis of hardness and strength by eliminating factors such as varying impurity contents and different heat treatments. Key findings, not presented in previous studies, are:

(i) The lowest hardness and RT strength among the alloy series is found for 42 at.% Al.
(ii) Fe-30Al and Fe-35Al display a YS peak at temperatures between 400 and 500 °C.
(iii) Strain hardening is consistently decreasing with increasing Al content.
(iv) Binary FeAl alloys show kink band formation during deformation.

Based on the results gained in this study, the following conclusions are drawn:

1. After the point defect-reducing heat treatment at 400 °C for 120 h, no YS peak was found in the present study for alloys with > 35 at.% Al. In the current study, a well-defined dwell time at the testing temperature was used, leading to different thermal vacancy concentrations prior to starting the test. These concentrations vary depending on Al concentration and on temperature due to the exponential temperature dependence of the kinetics. Previous reports on the YS peak in literature for higher Al contents can be explained by several factors, ranging from chemical inhomogeneity, the specific (thermo-)mechanical treatments and the distinct differentiation of $\sigma_f$ and $\sigma_y$. The findings from the current study suggest that the YS peak for Fe-30Al is caused by the growth of $D0_3$-ordered domains within *B*2-ordered grains. Further, the YS peak for Fe-35Al is explained by the strengthening effect of thermally generated vacancies. This effect becomes too high for alloys with Al contents >35at. % and raises the plateau strength above the YS peak level, hence, overshadowing the YS peak.
2. Thermally activated processes (dislocation cross slip and climb) and the increasing vacancy concentration with increasing Al content are the cause for the decreasing strain hardening capability with increasing temperatures in iron aluminides. Localization by kink band formaiton might also contribute to this as well. In general, deformation bands are found to occur at angles close to 45° with respect to the compression direction [81]. The appearance of kink bands found in the present study differs significantly from this angle, which is indicative of a superposition of kink band formation and uniform rotation of grains. Alloys with ≥ 47 at.% Al show low grain boundary strength and are not suitable for being subjected to tensile loads to probe the onset of plastic flow $\sigma_y$.

## Acknowledgements

We gratefully acknowledge financial support by the Deutsche Forschungsgemeinschaft (DFG) within the framework of the project no. 511095365 (HE1872/44-1 and KA4631/4-1 at KIT, STE1077/3-1 and BE7628/1-1 at MPI SusMat). This work was partly carried out with the support of the Karlsruhe Nano Micro Facility (KNMFi, proposal no. 2025-035-032491, www.knmf.kit.edu), a Helmholtz Research Infrastructure at Karlsruhe Institute of Technology (KIT, www.kit.edu). We acknowledge the chemical analysis by ICP-OES, CGHE and CA at the Institute for Applied Materials (IAM-AWP) by Dr. Bergfeldt, Karlsruhe Institute of Technology (KIT) and support by Dr. Anwesha Kanjilal (MPI SusMat) within the framework of this project.

## Conflict of Interest

The authors declare no conflict of interest.

## Data Availability Statement

The data presented in this study are available in Zenodo at https://doi.org/10.5281/zenodo.17510975, https://doi.org/10.5281/zenodo.17512156 and https://doi.org/10.5281/zenodo.17517632 under CC BY-SA 4.0 license. Further information is available upon request with alexander.kauffmann@rub.de.

## Author Contributions

Jan Lars Riedel: Investigation, Formal analysis, Software, Data Curation, Visualization, Project administration, Writing - Original Draft, Writing - Review & Editing

Alexander Kauffmann: Conceptualization, Investigation, Methodology, Formal analysis, Data Curation, Visualization, Supervision, Funding acquisition, Writing - Original Draft, Writing - Review & Editing

Stefan Guth: Investigation, Methodology, Formal analysis, Visualization, Supervision, Writing - Original Draft, Writing - Review & Editing

Marcel Münch: Methodology, Formal analysis, Visualization, Writing - Review & Editing

Georg Winkens: Formal analysis, Writing - Review & Editing

Daniel Schliephake: Formal analysis, Writing - Review & Editing

Jung Soo Lee: Investigation, Data Curation, Formal analysis, Writing - Review & Editing

James P. Best: Supervision, Resources, Methodology, Funding acquisition, Writing - Review & Editing

Frank Stein: Supervision, Resources, Funding acquisition, Writing - Review & Editing

Martin Heilmaier: Conceptualization, Supervision, Resources, Funding acquisition, Writing - Review & Editing

## References

[1] R.R. Judkins, U.S. Rao, Fossil energy applications of intermetallic alloys, Intermetallics 8 (2000) 1347–1354. https://doi.org/10.1016/S0966-9795(00)00110-2.

[2] M. Palm, F. Stein, G. Dehm, Iron Aluminides, Annual Review of Materials Research 49 (2019) 297–326. https://doi.org/10.1146/annurev-matsci-070218-125911.

[3] D.G. Morris, M.A. Muñoz-Morris, High temperature mechanical properties of iron aluminides, Revista de Metalurgia 37 (2001) 230–239. https://doi.org/10.3989/revmetalm.2001.v37.i2.471.

583 [4] M. Zamanzade, A. Barnoush, C. Motz, A Review on the Properties of Iron Aluminide
584 Intermetallics, Crystals 6 (2016) 10. https://doi.org/10.3390/cryst6010010.
585 [5] M. Palm, Fe–Al materials for structural applications at high temperatures: Current research at
586 MPIE, International Journal of Materials Research 100 (2009) 277–287.
587 https://doi.org/10.3139/146.110056.
588 [6] S.C. Deevi, Advanced intermetallic iron aluminide coatings for high temperature applications,
589 Progress in Materials Science 118 (2021) 100769. https://doi.org/10.1016/j.pmatsci.2020.100769.
590 [7] D.F.L. Borges, D.C.R. Espinosa, C.G. Schön, Making iron aluminides out of scrap, Journal of
591 Materials Research and Technology 3 (2014) 101–106.
592 https://doi.org/10.1016/j.jmrt.2013.12.002.
593 [8] J.W. Cohron, Y. Lin, R.H. Zee, E.P. George, Room-temperature mechanical behavior of FeAl:
594 effects of stoichiometry, environment, and boron addition, Acta Materialia 46 (1998) 6245–6256.
595 https://doi.org/10.1016/S1359-6454(98)00254-7.
596 [9] F. Stein, M. Palm, Re-determination of transition temperatures in the Fe–Al system by differential
597 thermal analysis, International Journal of Materials Research 98 (2007) 580–588.
598 https://doi.org/10.3139/146.101512.
599 [10] I. Baker, P.R. Munroe, Mechanical properties of FeAl, International Materials Reviews 42 (1997)
600 181–205. https://doi.org/10.1179/imr.1997.42.5.181.
601 [11] D. Risanti, J. Deges, L. Falat, S. Kobayashi, J. Konrad, M. Palm, B. Pöter, A. Schneider, C.
602 Stallybrass, F. Stein, Dependence of the brittle-to-ductile transition temperature (BDTT) on the Al
603 content of Fe–Al alloys, Intermetallics 13 (2005) 1337–1342.
604 https://doi.org/10.1016/j.intermet.2005.02.007.
605 [12] D. Rodney, J. Bonneville, Dislocations, in: Physical Metallurgy, Elsevier Amsterdam, 2014: pp.
606 1591–1680. https://doi.org/10.1016/B978-0-444-53770-6.00016-2.
607 [13] R.W. Cahn, P. Haasen, eds., Physical Metallurgy Vol. 3, 4th ed., Elsevier Science B.V.,
608 Amsterdam, 1996.
609 [14] E.P. George, I. Baker, Thermal vacancies and the yield anomaly of FeAl, Intermetallics 6 (1998)
610 759–763. https://doi.org/10.1016/S0966-9795(98)00063-6.
611 [15] H. Xiao, I. Baker, The temperature dependence of the flow and fracture of Fe-40Al, Scripta
612 Metallurgica et Materialia 28 (1993) 1411–1416. https://doi.org/10.1016/0956-716X(93)90491-
613 A.
614 [16] U. Reimann, G. Sauthoff, Effects of deviations from stoichiometry on the deformation behaviour
615 of FeAl at intermediate temperatures, Intermetallics 7 (1999) 437–445.
616 https://doi.org/10.1016/S0966-9795(98)00104-6.
617 [17] I. Baker, H. Xiao, O. Klein, C. Nelson, J.D. Whittenberger, The effect of temperature and Fe: Al
618 ratio on the flow and fracture of FeAl, Acta Metallurgica et Materialia 43 (1995) 1723–1730.
619 https://doi.org/10.1016/0956-7151(94)00369-S.
620 [18] K. Yoshimi, S. Hanada, H. Tokuno, Effect of Frozen-in Vacancies on Hardness and Tensile
621 Properties of Polycrystalline B2 FeAl, Materials Transactions, JIM 35 (1994) 51–57.
622 https://doi.org/10.2320/matertrans1989.35.51.
623 [19] E.P. George, I. Baker, A model for the yield strength anomaly of Fe-Al, Philosophical Magazine
624 A 77 (1998) 737–750. https://doi.org/10.1080/01418619808224080.
625 [20] P. Nagpal, I. Baker, Effect of cooling rate on hardness of FeAl and NiAl, Metallurgical
626 Transactions A 21 (1990) 2281–2282. https://doi.org/10.1007/BF02647891.
627 [21] M.A. Morris, O. George, D.G. Morris, Vacancies, vacancy aggregates and hardening in FeAl,
628 Materials Science and Engineering: A 258 (1998) 99–107. https://doi.org/10.1016/S0921-
629 5093(98)00922-8.
630 [22] M. Zhao, K. Yoshimi, K. Maruyama, K. Yubuta, Thermal vacancy behavior analysis through
631 thermal expansion, lattice parameter and elastic modulus measurements of B2-type FeAl, Acta
632 Materialia 64 (2014) 382–390. https://doi.org/10.1016/j.actamat.2013.10.051.
633 [23] K.-M. Chang, Tensile and impact properties of directionally solidified Fe-40Al intermetallic,
634 Metallurgical Transactions A 21 (1990) 3027–3028. https://doi.org/10.1007/BF02647223.
635 [24] M.A. Morris, D.G. Morris, Quenching and Ageing Effects on Defects and Their Structures in FeAl
636 Alloys, and the Influence on Hardening and Softening, Scripta Materialia 38 (1998) 509–516.
637 https://doi.org/10.1016/S1359-6462(97)00468-5.

[25] N.D. Diego, F. Plazaola, J.A. Jiménez, J. Serna, J.D. Río, A positron study of the defect structures in the D03 and B2 phases in the Fe–Al system, Acta Materialia 53 (2005) 163–172. https://doi.org/10.1016/j.actamat.2004.09.013.
[26] T. Haraguchi, F. Hori, R. Oshima, M. Kogachi, A study of vacancy-type defects in the B2-phase region of the Fe–Al system by positron annihilation method, Intermetallics 9 (2001) 763–770. https://doi.org/10.1016/S0966-9795(01)00061-9.
[27] J. Wolff, M. Franz, A. Broska, R. Kerl, M. Weinhagen, B. Köhler, M. Brauer, F. Faupel, Th. Hehenkamp, Point defects and their properties in FeAl and FeSi alloys, Intermetallics 7 (1999) 289–300. https://doi.org/10.1016/S0966-9795(98)00105-8.
[28] R. Würschum, C. Grupp, H. Schaefer, Simultaneous study of vacancy formation and migration at high temperatures in B2-type Fe aluminides, Physical Review Letters 75 (1995) 97–100. https://doi.org/10.1103/PhysRevLett.75.97.
[29] M. Kogachi, T. Haraguchi, Quenched-in vacancies in B2-structured intermetallic compound FeAl, Materials Science and Engineering: A 230 (1997) 124–131. https://doi.org/10.1016/S0921-5093(97)00016-6.
[30] E. Orowan, Fracture and strength of solids, Reports on Progress in Physics 12 (1949) 185–232. https://doi.org/10.1088/0034-4885/12/1/309.
[31] C.T. Liu, C.L. Fu, E.P. George, G.S. Painter, Environmental Embrittlement in FeAl Aluminides, ISIJ International 31 (1991) 1192–1200. https://doi.org/10.2355/isijinternational.31.1192.
[32] L.M. Pike, C.T. Liu, Environmental and Strain Rate Effects on the Ductility and Yield Strength of Fe-40Al, Scripta Materialia 38 (1998) 1475–1480. https://doi.org/10.1016/S1359-6462(98)00087-6.
[33] C.T. Liu, Recent advances in ordered intermetallics, Materials Chemistry and Physics 42 (1995) 77–86. https://doi.org/10.1016/0254-0584(95)01546-9.
[34] I. Baker, D.J. Gaydosh, Flow and fracture of FeAl, Materials Science and Engineering 96 (1987) 147–158. https://doi.org/10.1016/0025-5416(87)90549-0.
[35] M.A. Crimp, K. Vedula, Effect of boron on the tensile properties of B2 FeAl, Materials Science and Engineering 78 (1986) 193–200. https://doi.org/10.1016/0025-5416(86)90323-X.
[36] D.J. Gaydosh, S.L. Draper, R.D. Noebe, M.V. Nathal, Room temperature flow and fracture of Fe-40at.%Al alloys, Materials Science and Engineering: A 150 (1992) 7–20. https://doi.org/10.1016/0921-5093(90)90003-L.
[37] G. Hénaff, A. Tonneau, Environment-sensitive fracture of iron aluminides under monotonic tensile loading, Metall Mater Trans A 32 (2001) 557–567. https://doi.org/10.1007/s11661-001-0072-3.
[38] O. Klein, I. Baker, The effect of boron on the temperature dependence of the flow and fracture of Fe45Al, Scripta Metallurgica et Materialia 30 (1994) 1413–1417. https://doi.org/10.1016/0956-716X(94)90238-0.
[39] D.G. Morris, J. Chao, C.G. Oca, M.A. Muñoz-Morris, Obtaining good ductility in an FeAl intermetallic, Materials Science and Engineering: A 339 (2003) 232–240. https://doi.org/10.1016/S0921-5093(02)00108-9.
[40] P. Nagpal, I. Baker, The effect of strain rate on the room-temperature ductility of FeAl, Scripta Metallurgica et Materialia 25 (1991) 2577–2580. https://doi.org/10.1016/0956-716X(91)90071-8.
[41] D. Wu, I. Baker, The effect of environment and strain rate on the room temperature tensile properties of FeAl single crystals, Intermetallics 9 (2001) 57–65. https://doi.org/10.1016/S0966-9795(00)00097-2.
[42] Y. Yang, I. Baker, E.P. George, Effect of Vacancies on the Tensile Properties of Fe-40Al Single Crystals in Air and Vacuum, Materials Characterization 42 (1999) 161–167. https://doi.org/10.1016/S1044-5803(98)00049-7.
[43] K. Yoshimi, S. Hanada, Positive temperature dependence of yield stress in B2 FeAl, in: Proceedings of the First International Symposium on Structural Intermetallics, Publ by Minerals, Metals & Materials Soc (TMS), Champion, PA, USA, 1993: pp. 475–482.
[44] K. Yoshimi, S. Hanada, M.H. Yoo, Tensile properties of B2-type Fe-39mol%Al single crystals at elevated temperatures, Intermetallics 4 (1996) 159–168. https://doi.org/10.1016/0966-9795(95)00032-1.
[45] K. Yoshimi, S. Hanada, M.H. Yoo, Yield Stress Anomaly in B2 FeAl, MRS Proceedings 460 (1996) 313. https://doi.org/10.1557/PROC-460-313.

[46] O. Klein, I. Baker, Effect of heat-treatment on the tensile behavior of iron-rich FeAl and FeAl + B, Scripta Metallurgica et Materialia 30 (1994) 627–632. https://doi.org/10.1016/0956-716X(94)90441-3.
[47] P. Nagpal, I. Baker, Room temperature fracture of FeAl and NiAl, Materials Characterization 27 (1991) 167–173. https://doi.org/10.1016/1044-5803(91)90060-H.
[48] C.T. Liu, E.H. Lee, C.G. McKamey, An environmental effect as the major cause for room-temperature embrittlement in FeAl, Scripta Metallurgica 23 (1989) 875–880. https://doi.org/10.1016/0036-9748(89)90263-9.
[49] R. Kerl, J. Wolff, Th. Hehenkamp, Equilibrium vacancy concentrations in FeAl and FeSi investigated with an absolute technique, Intermetallics 7 (1999) 301–308. https://doi.org/10.1016/S0966-9795(98)00118-6.
[50] J.B. Nelson, D.P. Riley, An experimental investigation of extrapolation methods in the derivation of accurate unit-cell dimensions of crystals, Proc. Phys. Soc. 57 (1945) 160–177. https://doi.org/10.1088/0959-5309/57/3/302.
[51] L. Spieß, G. Teichert, R. Schwarzer, H. Behnken, C. Genzel, Moderne Röntgenbeugung, Springer Fachmedien Wiesbaden, Wiesbaden, 2019. https://doi.org/10.1007/978-3-8348-8232-5.
[52] F. Bachmann, R. Hielscher, H. Schaeben, Texture Analysis with MTEX – Free and Open Source Software Toolbox, Solid State Phenomena 160 (2010) 63–68. https://doi.org/10.4028/www.scientific.net/SSP.160.63.
[53] DIN EN ISO 6507-1:2024-01, Metallische Werkstoffe_- Härteprüfung nach Vickers_- Teil_1: Prüfverfahren (ISO_6507-1:2023); Deutsche Fassung EN_ISO_6507-1:2023, (n.d.). https://doi.org/10.31030/3503781.
[54] W.C. Oliver, G.M. Pharr, An improved technique for determining hardness and elastic modulus using load and displacement sensing indentation experiments, Journal of Materials Research 7 (1992) 1564–1583. https://doi.org/10.1557/JMR.1992.1564.
[55] W.C. Oliver, G.M. Pharr, Measurement of hardness and elastic modulus by instrumented indentation: Advances in understanding and refinements to methodology, Journal of Materials Research 19 (2004) 3–20. https://doi.org/10.1557/jmr.2004.19.1.3.
[56] H. Xiao, I. Baker, The relationship between point defects and mechanical properties in Fe-Al at room temperature, Acta Metallurgica et Materialia 43 (1995) 391–396. https://doi.org/10.1016/0956-7151(95)90295-3.
[57] M. Kogachi, T. Haraguchi, Random vacancy distribution in B2-type intermetallic compound FeAl, Scripta Materialia 39 (1998) 159–165. https://doi.org/10.1016/S1359-6462(98)00145-6.
[58] J. Wolff, M. Franz, A. Broska, B. Köhler, Th. Hehenkamp, Defect types and defect properties in FeAl alloys, Materials Science and Engineering: A 239–240 (1997) 213–219. https://doi.org/10.1016/S0921-5093(97)00584-4.
[59] J. Wolff, M. Franz, T. Hehenkamp, Defect analysis with positron annihilation Applications to Fe aluminides, Mikrochim Acta 125 (1997) 263–268. https://doi.org/10.1007/BF01246194.
[60] Y.A. Chang, L.M. Pike, C.T. Liu, A.R. Bilbrey, D.S. Stone, Correlation of the hardness and vacancy concentration in FeAl, Intermetallics 1 (1993) 107–115. https://doi.org/10.1016/0966-9795(93)90028-T.
[61] J.L. Riedel, A. Kauffmann, S. Guth, M. Muench, G. Winkens, D. Schliephake, J.S. Lee, J.P. Best, F. Stein, M. Heilmaier, Evaluated data from "Re-Assessing the Strength and Deformation Behavior of B2-ordered Binary Iron Aluminides," (2025). https://doi.org/10.5281/ZENODO.17517632.
[62] J.L. Riedel, A. Kauffmann, S. Guth, M. Muench, G. Winkens, D. Schliephake, J.S. Lee, J.P. Best, F. Stein, M. Heilmaier, Mechanical test data from "Re-Assessing the Strength and Deformation Behavior of B2-ordered Binary Iron Aluminides," (2025). https://doi.org/10.5281/ZENODO.17510975.
[63] H. Mecking, U.F. Kocks, Kinetics of flow and strain-hardening, Acta Metallurgica 29 (1981) 1865–1875. https://doi.org/10.1016/0001-6160(81)90112-7.
[64] Y. Yang, I. Baker, The influence of vacancy concentration on the mechanical behavior of Fe-40Al, Intermetallics 6 (1998) 167–175. https://doi.org/10.1016/S0966-9795(97)00062-9.
[65] S. Nizamoglu, A. Gedsun, Kauffmann, A., M. Ghosh, H. Michels, T. Groten, C. Schulz, C. Breuner, S. Seils, D. Schliephake, S. Laube, M. Palm, M. Heilmaier, Microstructure and

Mechanical Properties of a Precipitation-Strengthened Fe–Al–Nb Alloy, Advanced Engineering Materials (2023) 2300148.
[66] D. Tabor, The hardness of solids, Reviews of Physics in Technology 1 (1970) 145–179. https://doi.org/10.1088/0034-6683/1/3/I01.
[67] G. Winkens, A. Kauffmann, J. Herrmann, A.K. Czerny, S. Obert, S. Seils, T. Boll, C. Baruffi, Y. Rao, W.A. Curtin, R. Schwaiger, M. Heilmaier, The influence of lattice misfit on screw and edge dislocation-controlled solid solution strengthening in Mo-Ti alloys, Communications Materials 4 (2023) 26. https://doi.org/10.1038/s43246-023-00353-8.
[68] F.J. Humphreys, M. Hatherly, Recrystallization and related annealing phenomena, 2nd ed., Elsevier, Amsterdam, 2004.
[69] D.B. Miracle, O.N. Senkov, C. Frey, S. Rao, T.M. Pollock, Strength vs temperature for refractory complex concentrated alloys (RCCAs): A critical comparison with refractory BCC elements and dilute alloys, Acta Materialia 266 (2024) 119692. https://doi.org/10.1016/j.actamat.2024.119692.
[70] A. Schmitt, K.S. Kumar, A. Kauffmann, M. Heilmaier, Microstructural evolution during creep of lamellar eutectoid and off-eutectoid FeAl/FeAl2 alloys, Intermetallics 107 (2019) 116–125. https://doi.org/10.1016/j.intermet.2019.01.015.
[71] G. Gottstein, Physical Foundations of Materials Science, Springer Berlin Heidelberg, Berlin, Heidelberg, 2004. https://doi.org/10.1007/978-3-662-09291-0.
[72] H.-E. Schaefer, B. Damson, M. Weller, E. Arzt, E.P. George, Thermal Vacancies and High-Temperature Mechanical Properties of FeAl, Phys. Stat. Sol. (a) 160 (1997) 531–540. https://doi.org/10.1002/1521-396X(199704)160:2%253C531::AID-PSSA531%253E3.0.CO;2-7.
[73] R. Osmundsen, I. Baker, The Effect of Antiphase Boundary Tubes on the Hardness of FeAl, Metall Mater Trans A 52 (2021) 3694–3698. https://doi.org/10.1007/s11661-021-06355-w.
[74] J.S. Lee, J.L. Riedel, P. Schweizer, A. Kauffmann, M. Heilmaier, G. Dehm, J.P. Best, A. Kanjilal, F. Stein, Influence of point defects on the hardness and reduced modulus of B2-ordered FeAl, Manuscript Submitted to Journal of Alloys and Compounds (2026).
[75] F. Stein, Selected Al-Fe-X ternary systems for industrial applications, MSI Science Simplified, Stuttgart, 2022.
[76] T. Hehenkamp, P. Scholz, B. Köhler, R. Kerl, Vacancy Formation and Diffusion in FeAl-Alloys, DDF 194–199 (2001) 389–396. https://doi.org/10.4028/www.scientific.net/DDF.194-199.389.
[77] L.M. Pike, Y.A. Chang, C.T. Liu, Point defect concentrations and hardening in binary B2 intermetallics, Acta Materialia 45 (1997) 3709–3719. https://doi.org/10.1016/S1359-6454(97)00028-1.
[78] I. Baker, X. Li, H. Xiao, R. Carleton, E.P. George, The room temperature strengthening effect of boron as a function of aluminum concentration in FeAl, Intermetallics 6 (1998) 177–183. https://doi.org/10.1016/S0966-9795(97)00063-0.
[79] W.D. Nix, H. Gao, Indentation size effects in crystalline materials: A law for strain gradient plasticity, Journal of the Mechanics and Physics of Solids 46 (1998) 411–425. https://doi.org/10.1016/S0022-5096(97)00086-0.
[80] P. Kratochvíl, J. Kopeček, J. Pešička, G. Schmitz, The effect of annealing at temperatures near B2⇔D03 transformation in Fe3Al-type alloy on the yield stress, Intermetallics 8 (2000) 121–123. https://doi.org/10.1016/S0966-9795(99)00074-6.
[81] D. Kuhlmann-Wilsdorf, Overview No. 131 “Regular” deformation bands (DBs) and the LEDS hypothesis, Acta Materialia 47 (1999) 1697–1712. https://doi.org/10.1016/S1359-6454(98)00413-3.
[82] M.R. Drury, F.J. Humphreys, The development of microstructure in Al-5% Mg during high temperature deformation, Acta Metallurgica 34 (1986) 2259–2271. https://doi.org/10.1016/0001-6160(86)90171-9.
[83] F.J. Humphreys, P.B. Prangnell, J.R. Bowen, A. Gholinia, C. Harris, Developing stable fine-grain microstructures by large strain deformation, Philosophical Transactions: Mathematical, Physical and Engineering Sciences 357 (1999) 1663–1681. https://doi.org/10.1098/rsta.1999.0395.
[84] I. Baker, A review of the mechanical properties of B2 compounds, Materials Science and Engineering: A 192–193 (1995) 1–13. https://doi.org/10.1016/0921-5093(94)03200-9.
[85] D.G. Morris, M.A. Morris, Strengthening at intermediate temperatures in iron aluminides, Materials Science and Engineering: A 239–240 (1997) 23–38. https://doi.org/10.1016/S0921-5093(97)00557-1.

805 [86] Y. Umakoshi, M. Yamaguchi, Deformation of FeAl single crystals at high temperatures,
806 Philosophical Magazine A 41 (1980) 573–588. https://doi.org/10.1080/01418618008239334.
807 [87] I. Baker, Y. Yang, On the yield stress anomaly in stoichiometric FeAl, Materials Science and
808 Engineering: A 239–240 (1997) 109–117. https://doi.org/10.1016/S0921-5093(97)00568-6.
809 [88] M. Kupka, High temperature strengthening of the FeAl intermetallic phase-based alloy,
810 Intermetallics 14 (2006) 149–155. https://doi.org/10.1016/j.intermet.2005.04.013.
811 [89] D.G. Morris, C.T. Liu, E.P. George, Pinning of dislocations and the origin of the stress anomaly
812 in FeAl alloys, Intermetallics 7 (1999) 1059–1068. https://doi.org/10.1016/S0966-
813 9795(99)00015-1.
814 [90] D.G. Morris, J.C. Joye, M. Leboeuf, Hardening and strain-ageing by vacancies and their
815 aggregates in FeAl, Phil. Mag. A 69 (1994) 961–980.
816 https://doi.org/10.1080/01418619408242530.
817 [91] N. Junqua, J.C. Desoyer, P. Moine, Electron microscopy observation of quenching defects in an
818 ordered alloy of B2 type: Fe–40 at% Al, Phys. Stat. Sol. (a) 18 (1973) 387–395.
819 https://doi.org/10.1002/pssa.2210180139.
820 [92] D.G. Morris, M.A. Muñoz-Morris, L.M. Requejo, Work hardening in Fe–Al alloys, Materials
821 Science and Engineering: A 460–461 (2007) 163–173.
822 https://doi.org/10.1016/j.msea.2007.01.014.
823 [93] P.R. Munroe, I. Baker, The microstructure of extruded Fe-Al, J Mater Sci 24 (1989) 4246–4252.
824 https://doi.org/10.1007/BF00544494.
825